Geometrical Analysis of Station-Keeping Strategies About Libration Point Orbits

Ariadna Farrés*
NASA Goddard Space Flight Center, 20771 Greenbelt, Maryland
Chen Gao†
Northwestern Polytechnical University, 710060 Xi'an, People's Republic of China
Josep J. Masdemont‡
Polytechnic University of Catalonia, 08034 Barcelona, Spain
Gerard Gómez§
University of Barcelona, 08007 Barcelona, Spain
and
David C. Folta¶ and Cassandra Webster**
NASA Goddard Space Flight Center, 20771 Greenbelt, Maryland

https://doi.org/10.2514/1.G006014

Throughout the years, different strategies have been proposed for the station-keeping around the libration point orbits. In this paper, a geometrical comparative analysis is performed between different approaches making use of the Floquet modes reference frame. Two particular station-keeping procedures are considered: the commonly used velocity constraint at the plane crossing, and the Floquet mode approach. The first method finds the Δv that ensures that the x component of the velocity vector is zero at a plane crossing, whereas the Floquet mode approach finds the Δv that cancels the unstable mode in the Floquet reference frame. It will be seen that both approaches have some basic common geometrical features, even when they are compared using high-order techniques.

I. Introduction

THE basic purpose of station-keeping is to maintain a spacecraft within a predefined neighborhood about a nominal path. It is defined as a control procedure that seeks to minimize some combination of the deviation of the spacecraft from the nominal trajectory and the total maneuver cost, which can be subjected to constraints such as the minimum time interval between two consecutive maneuvers or the maximum fuel expenditure at each maneuver. Assuming discrete and impulsive corrections, the problem is the determination of the suitable maneuvers, including their magnitude, direction, and timing.

The motion of a spacecraft near the L_1 or L_2 collinear libration points in the sun–Earth or in the Earth–moon systems is very unstable, so a spacecraft has to perform correction maneuvers to remain in a libration point orbit (LPO), taking into account errors in orbit determination, and maneuver executions. Since the first libration point satellite, the International Sun-Earth Explorer 3 (ISEE-3), several station-keeping techniques have been developed for LPO, the first ones being credited to Farquhar [1] and Breakwell et al. [2]. The cornerstone ISEE-3 mission used a nominal path close to an approximated periodic halo orbit around the L_1 point with a period of six months; for the station-keeping a series of maneuvers were executed approximately every three months, each one with an averaged Δv magnitude of 2 m/s (see [3,4]). The Solar & Heliospheric Observatory (SOHO) spacecraft, which was the second sun–Earth L_1 LPO mission, used a similar nominal orbit, but the high sensitivity of its instrumentation required the station-keeping maneuvers to be small; hence it was not possible to use the same control strategy as for the ISEE-3. Studies done by the European Space Agency [5–7] showed that, with an average time interval between maneuvers of also three months, the station-keeping is possible with 50 cm/s per year. This value is of the same order of magnitude as the results obtained later by Howell and her collaborators using a different strategy [8–10].

One of the key points for most station-keeping strategies is to use an accurate reference trajectory. This orbit is determined using a force model for the motion of the spacecraft that must be as close as possible to the "real" one. Unmodeled perturbations, as well as any orbit injection error, will result in a deviation of the spacecraft from the nominal path, and the unstable nature of LPOs will further amplify it. Using a halo-type orbit as a nominal path, for both sun–Earth and the Earth–moon systems, the amplification factor for deviation errors is about 1500 per revolution. Under these conditions, a spacecraft without any control is going to escape from the neighborhood of the reference orbit in less than 180 or 14 days, respectively, even with very small initial errors. In the 1980s, the Barcelona Dynamical Systems Group developed a station-keeping strategy using dynamic systems tools to find the minimum Δv to remain close to periodic and quasi-periodic orbits. Their strategy, also known as Floquet mode approach, uses the Floquet base to describe the linear dynamics in the vicinity of the orbit, and finds the minimum $\Delta \boldsymbol{v}$ that cancels the instability. From the operational point of view, a drawback of the procedure is that it requires an accurate reference orbit, which adds some extra complexity.

Missions like the Advanced Composition Explorer (ACE), and the Global Geospace Science Wind consider a different station-keeping procedure that avoids the use of an accurate nominal orbit [11,12]. In this method, each maneuver $\Delta \boldsymbol{v}$ is designed to ensure that, if the trajectory is propagated for one or two additional revolutions, the x component of the velocity vector is zero when crossing the $y = 0$

Received 24 February 2021; revision received 1 December 2021; accepted for publication 2 December 2021; published online 14 February 2022.

*Science Collaborator, University of Maryland Baltimore County; ariadna.farresbasiaba@nasa.gov.

†Ph.D. Student, Shaanxi, National Key Laboratory of Aerospace Flight Dynamics and Polytechnic University of Catalonia; chen.gao@upc.edu.

‡Professor, Institute of Space Studies of Catalonia (IEEC) and Institute of Mathematics of UPC-Barcelona Tech (IMTech); josep.masdemont@upc.edu.

§Professor, Institute of Space Studies of Catalonia (IEEC); gerard@maia.ub.es.

¶Aerospace Engineer; david.c.folta@nasa.gov. Senior Fellow AIAA.

**Roman Space Telescope (RST) Flight Dynamics Lead; cassandra.webster@nasa.gov.

plane in the rotation libration point reference frame (RLP). Thanks to the symmetries in the circular restricted three-body problem (CRTBP), this condition ensures that the spacecraft is close to an LPO and will continue orbiting around the libration point over the next orbital periods. An improvement of this strategy was used for the Acceleration, Reconnection, Turbulence and Electrodynamics of Moon's Interaction with the Sun Mission (ARTEMIS) [13,14], where an optimization routine was used to find the maneuver direction and location that would minimize the $\Delta \boldsymbol{v}$ to meet $V_x = \pm 10$ cm/s at the 4th RLP $y = 0$ plane crossing. This kind of strategies is also being considered for the station-keeping design for future LPO missions, like the James Webb Space Telescope (JWST) [15] and the Roman Space Telescope (RST) (previously known as the Wide Fields Infra-Red Survey Telescope (WFIRST)) [16,17].

In the literature, there are several review papers that compare station-keeping strategies (see [13,18–20]); most of them focus on comparing the total cost and performance between them. The aim of this paper is to describe and compare two of these strategies from a geometrical and dynamic point of view, trying to understand their differences and nature. Understanding the geometry of a station-keeping strategy is important because it helps describe the impact that mission constraints have on the magnitude of $\Delta \boldsymbol{v}$ maneuvers. We have chosen the x-axis velocity constraint at plane crossing because of its relevance and use in past and future mission applications, and the Floquet mode station-keeping because of its geometrical definition and independence with respect to any optimization method. All the analysis and simulations are done using the CRTBP as the dynamic model that, as it is well known, captures most of the fundamental dynamics of a full ephemeris model around the libration points considered. However, the methods and results presented here can be easily extended to higher-fidelity force models. We use the Floquet mode reference frame to describe the motion of the spacecraft's trajectory around an LPO because it gives insight on the dynamic and geometrical behavior of a given station-keeping strategy. All the station-keeping maneuvers are modeled as instantaneous changes in velocity and can be seen as a jump in the phase space.

As we will see, both station-keeping strategies share a common geometric interpretation despite following different approaches. In both cases, the projection of the deviations of the trajectory from a nominal orbit on the Floquet mode reference frame shows that the $\Delta \boldsymbol{v}$ maneuvers bring the spacecraft toward the stable manifolds. Moreover, the jet transport procedure [21,22] provides semi-analytic expressions of both controllers, allowing to compare the geometry of both strategies and perform long-term stability analyses.

Understanding the geometry of these strategies allows the study of the optimality of the $\Delta \boldsymbol{v}$ maneuvers analytically. In this paper, we show why the minimum thrust direction is close to the position components of the stable eigenvector. We also describe the dependence of the maneuver size as a function of the thrust direction, and provide a tool to describe the impact of mission constraints in the thrust directions. Moreover, the geometric interpretation of station-keeping allows us to envision strategies that can help to mitigate the impact of mission constraints, such as actively biasing the $\Delta \boldsymbol{v}$ maneuvers when the spacecraft can only thrust away from the sun.

This paper is organized as follows: Section II provides a short review of the CRTBP, together with different kinds of LPOs and the linear approximation of the dynamics around them. The station-keeping strategies are explained in Sec. III, including the types of maneuvers and controllers used in the simulations. Since most of the simulations and dynamic analysis have been done using high-order Taylor expansions, for both the flow map and the functions required for the maneuvers, we include in Sec. IV a short explanation of the jet transport procedure used for these computations. This procedure allows us to compute high-order expansions of the flow of ordinary differential equations using automatic differentiation techniques. All the strategies are compared in detail in Sec. V. Section V.A provides the geometrical analysis of the station-keeping procedures, together with the effect of the different control parameters on the resulting trajectory, as well as on the total fuel consumption. Section V.B compares both strategies using Poincaré map simulations, and Sec. V.C is devoted to the long-term stability analysis of the control procedures by means of the definition of suitable Poincaré maps. In Sec. VI, the optimality of the station-keeping strategy is discussed analyzing the effect of varying some basic control parameters. Finally, in Sec. VII we give the final conclusions.

II. Libration Point Orbits of the Circular Restricted Three-Body Problem

The analysis and simulations in this paper have been carried out in the sun–Earth CRTBP, which maintains the most relevant dynamic properties of the real problem. However, the ideas and results can be extended to other models, including n-body problems using numerical ephemeris for the computation of the positions of the solar system bodies.

Recall that the equations of motion for a spacecraft in the CRTBP taking a rotating reference frame and using normalized units are written as

$$\ddot{x} - 2\dot{y} = \frac{\partial \Omega}{\partial x}, \qquad \ddot{y} + 2\dot{x} = \frac{\partial \Omega}{\partial y}, \qquad \ddot{z} = \frac{\partial \Omega}{\partial z} \tag{1}$$

where $\Omega(x, y, z) = (1/2)(x^2 + y^2) + ((1-\mu)/r_{ps}) + (\mu/r_{pe})$, in which $r_{ps} = \sqrt{(x+\mu)^2 + y^2 + z^2}$ and $r_{pe} = \sqrt{(x+\mu-1)^2 + y^2 + z^2}$ are the sun–spacecraft and Earth–spacecraft distances, respectively.

The rotating reference frame has the origin at the center of mass of the sun–Earth system, the two primaries are fixed on the x axis, the z axis is perpendicular to the ecliptic plane, and the y axis completes an orthogonal positive oriented reference system. The normalized units of mass, distance, and time (see [23], Chapter 1) are chosen so that the total mass of the system and the distance between the two primaries are both equal to one, and the sun–Earth orbital period is 2π. In the paper, we use km and m/s to plot the trajectories, and normalized units to plot variation in the Floquet modes reference frame.

A. Libration Point Orbits and Their Neighborhood

In the CRTBP, there are different kinds of LPOs around the collinear equilibrium points, including halo, quasi-halo, near-rectilinear halo, and Lissajous orbits. The pioneering work of Farquhar [1] on halo orbits, around the L_1 and L_2 libration points, was followed by the work of Richardson [24,25] with a third-order analytical theory for their computation using the Lindstedt–Poincaré method. This theory was formulated in a synodical dimensionless coordinate system centered at the libration point under consideration. The same method was used by Farquhar and Kamel [26], and later by Richardson and Cary [27], to get low-order Lissajous-type solutions. The organization in the phase space of these different kinds of solutions was clear after the work of Gómez et al. [28], where a detailed study of the phase space in a large vicinity around the collinear equilibrium points was done, as well as the extension up to a high-order (25) of the Lindstedt–Poincaré series associated to halo and Lissajous orbits. The normal form computations revealed the existence of the so-called quasi-halo orbits, two-dimensional tori around the usual periodic halo orbits, that also play a relevant role in the phase space structure. The semi-analytical computation of this new kind of solutions was done in [29].

The different kinds of LPOs can be (and have been) used as nominal trajectories for libration point missions. As it has already been said, halo orbits were used by the ISEE-3 and the SOHO spacecraft, and a Lissajous orbit was used by ACE and, recently, by the Deep Space Climate Observatory (DSCOVR) [30]. Quasi-halo orbits are good nominal orbits for constellations of spacecraft, as it was proposed in the past for the Terrestrial Planet Finder (TPF) mission [31]. To maximize the launch window opportunities for the JWST, a large variety of target orbits have been considered, varying from tight halo orbits to wide quasi-halo orbits, or even large Lissajous orbits. On the other hand, due to mission requirement, RST is restricted to follow a small quasi-halo orbit.

The understanding of the local behavior of the flow associated to the dynamic model near an orbit is basic for the study of the station-keeping, as well as the effect of the different error sources on it. For any of the three main different kinds of LPOs, the basic point is to split the phase space into the center, stable and unstable parts of the tangent and normal spaces to any of the above-mentioned solutions (periodic halo orbits or two-dimensional tori). This splitting is clear in the periodic case: for a halo orbit (of moderate size), its monodromy matrix [i.e., the state transition matrix $A(t)$ at time T] contains three different blocks:

i) First is a diagonal block associated to the hyperbolic plane is one of them.

ii) Next is a block corresponding to a rotation, where the mean angular velocity of this rotation is the normal frequency.

iii) Third is a block with a double eigenvalue equal to one, and nonzero out of diagonal term (related to the variation of the period of the orbit along the family). The eigenvector corresponds to a time (phase) shift along the orbit, while the other vector corresponds to energy variations along the family of halo orbits.

The eigenspace of the first block corresponds to the unstable and stable manifolds, whereas the eigenspace associated to the last two blocks contains the center behavior around the orbit, that is, its center manifold. In the case of a nominal Lissajous or quasi-halo orbit, one cannot talk about the monodromy matrix, since the variational equations are not periodic. However, assuming reducibility of these equations to constant coefficients [32], one can still find the first block, and instead of blocks (ii) and (iii), there is a 4×4 block associated to an eigenvalue equal to one, with two eigenvectors that correspond to phase shifts and the other two vectors are associated to variations of the frequencies corresponding to variations of the amplitudes of the torus.

In the case of a halo orbit, the two-dimensional unstable manifold and the two-dimensional stable manifold can be easily computed from the monodromy matrix M. The eigenvalues λ_i $(i = 1, \ldots, 6)$ of M are such that $\lambda_1 > 1$; $\lambda_2 = 1/\lambda_1$ and $\lambda_3 = \overline{\lambda_4}$ are both complex of module one; and $\lambda_5 = \lambda_6 = 1$.

If $\boldsymbol{e}_1(0)$ is the eigenvector related to $\lambda_1 > 1$, then the vector $\boldsymbol{e}_1(t) = A(t)\boldsymbol{e}_1(0)$, together with the tangent vector to the orbit $\boldsymbol{e}_5(t)$, spans the tangent plane to the local unstable manifold. In a similar way, $\boldsymbol{e}_2(t)$ can be computed and used to determine the linear approximation of the stable manifold. From these two vectors, one can compute the corresponding Floquet modes (see [6]) as

$$\overline{\boldsymbol{e}}_i(t) = \boldsymbol{e}_i(t) \exp\left(-t \frac{\ell_n \lambda_i}{T}\right), \qquad i = 1, 2 \tag{2}$$

where T is the period of the orbit. If $\boldsymbol{e}_3(0) + i\boldsymbol{e}_4(0)$ is the complex eigenvector related to λ_3, and $\boldsymbol{e}_3(t) + i\boldsymbol{e}_4(t) = A(t)(\boldsymbol{e}_3(0) + i\boldsymbol{e}_4(0))$, then

$$\overline{\boldsymbol{e}}_3(t) = \cos\left(-t\frac{\Gamma}{T}\right)\boldsymbol{e}_3(t) - \sin\left(-t\frac{\Gamma}{T}\right)\boldsymbol{e}_4(t) \tag{3}$$

$$\overline{\boldsymbol{e}}_4(t) = \sin\left(-t\frac{\Gamma}{T}\right)\boldsymbol{e}_3(t) + \cos\left(-t\frac{\Gamma}{T}\right)\boldsymbol{e}_4(t) \tag{4}$$

where, if r is the real part of λ_3, then $\Gamma = \arccos r - 2\pi$.

The fifth mode is the vector tangent to the orbit and, as it is periodic, coincides with the corresponding Floquet mode $\overline{\boldsymbol{e}}_5(t) = \boldsymbol{e}_5(t)$. The vector tangent to the family is $\boldsymbol{e}_6(t)$, from which it is easy to compute the last Floquet mode $\overline{\boldsymbol{e}}_6(t)$ (see [6]).

B. Floquet Modes to Describe the Motion Around Libration Point Orbits

The Floquet modes allow the description of the natural dynamics in the vicinity of a periodic orbit. They can be used to define a periodic reference frame around an LPO in which the dynamics close to the orbit is simple to describe. On the planes generated by $\overline{\boldsymbol{e}}_1(t)$ and $\overline{\boldsymbol{e}}_2(t)$, the motion is of the saddle type: trajectories close to the halo orbit escape with an exponential rate along the unstable direction; on the planes generated by $\overline{\boldsymbol{e}}_3(t), \overline{\boldsymbol{e}}_4(t)$, the dynamics consists of a rotation around the periodic orbit; and on the planes generated by $\overline{\boldsymbol{e}}_5(t), \overline{\boldsymbol{e}}_6(t)$, the dynamics is neutral. Moreover, since the Floquet modes are periodic, they can be easily represented by their Fourier series.

The Floquet mode reference frame not only gives a good description of the motion near an LPO, but can also be used to design a station-keeping strategy [6,33,34], according to the following general ideas. At a given epoch, one can define the state error of a spacecraft as the difference between its actual state and a nominal one on the reference LPO. The evolution of this error can be approximated using the variational equations and can be represented using the basis defined by the Floquet modes. As it has already been said, the component of a deviation error along the unstable mode $\overline{\boldsymbol{e}}_1(t)$ has an exponential behavior and at each revolution, this component is multiplied by a factor equal to the corresponding eigenvalue (which in the typical examples is of the order of 10^3). The second Floquet mode is stable, and deviations with respect to this mode decrease exponentially with time. The remaining four modes, associated to eigenvalues of modulus equal to one, are neutral. In the so-called Floquet station-keeping strategy, maneuvers are performed to take care of the unstable mode $\overline{\boldsymbol{e}}_1(t)$.

The nominal point used to define the state deviation can be chosen in different ways: for instance, as the point of the nominal orbit at minimum distance from the detected position of the spacecraft in the configuration space (closest in position), or as the point at minimum distance in the phase space (closest in position and velocity), or as the point of the nominal orbit isochronous with the spacecraft, etc. In practice, there is not much difference between these nominal points; hence in what follows we use the isochronous one. The main advantage of the isochronous point is that it can be trivially computed.

The first row of Fig. 1 (whose details will be explained in detail in Sec. V) shows (in adimensional units [DU]) the evolution of the six Floquet components starting from a small deviation in the initial conditions of a periodic halo orbit. The second row of the same figure gives an insight of how the Floquet mode station-keeping strategy, which is going to be defined in Sec. III, takes care of the evolution of the unstable behavior. Note that each station-keeping maneuver is visualized as a jump in the phase space and is indicated with an arrow in the plot.

III. Two Station-Keeping Strategies

At a given epoch, the position and velocity of a spacecraft are estimated using tracking data, which, due to errors, give approximated values for both quantities. Errors in the injection into the nominal orbit, in the execution of the station-keeping maneuvers, and in the dynamic model used for the computation of the nominal trajectory, add inaccuracies when determining the spacecraft nominal orbit. All these facts have to be taken into account in the design of a station-keeping strategy.

Generally, when we detect that the spacecraft departs from the nominal orbit, it is not necessary to return to the nominal orbit; what must be done is to cancel the unstable component of the deviation to ensure that the spacecraft continues orbiting around the libration point. There are different ways to control this instability; in this paper, we analyze two different approaches:

1) *The Floquet mode approach (FM)*, which finds the $\Delta \boldsymbol{v}$ that cancels the unstable component in the Floquet reference frame. The underlying idea of this strategy is to cancel the deviation with respect to the nominal orbit [35,36].

2) *The velocity constraint approach (VX0)*, which finds the $\Delta \boldsymbol{v}$ that ensures that after about 1.5 orbital revolutions, the $\dot{x}$ component of the trajectory when crossing the $y = 0$ RLP plane is zero ($\dot{x} = 0$). The underlying idea of this strategy is to keep orbiting about the libration point [18].

A. Floquet Mode Approach

Let $\boldsymbol{\delta} = (\delta x, \delta y, \delta z, \delta \dot{x}, \delta \dot{y}, \delta \dot{z})^T$ be a deviation vector, that is, the difference between the state of the spacecraft computed from the tracking data and the nominal point on the nominal orbit. At a given

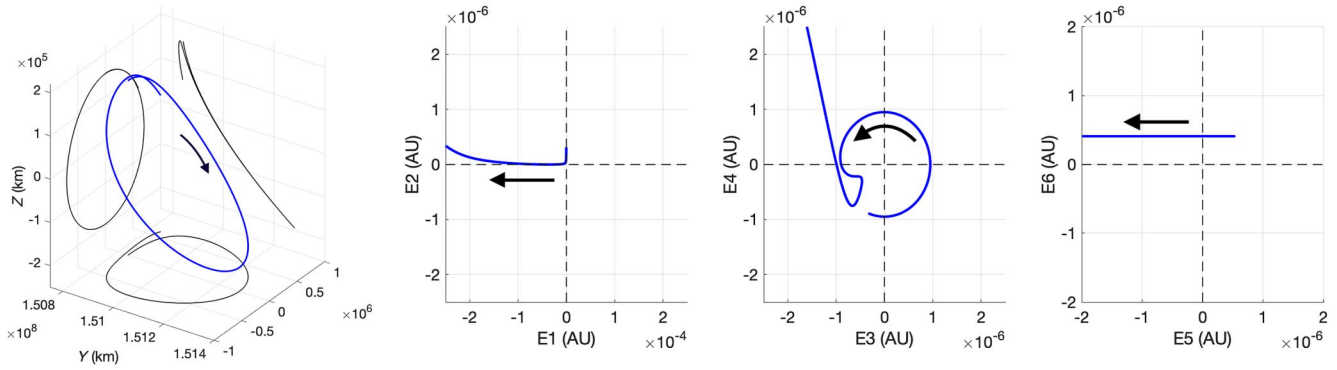

a) Evolution of the Floquet components for a trajectory close to halo orbit with no station-keeping maneuvers

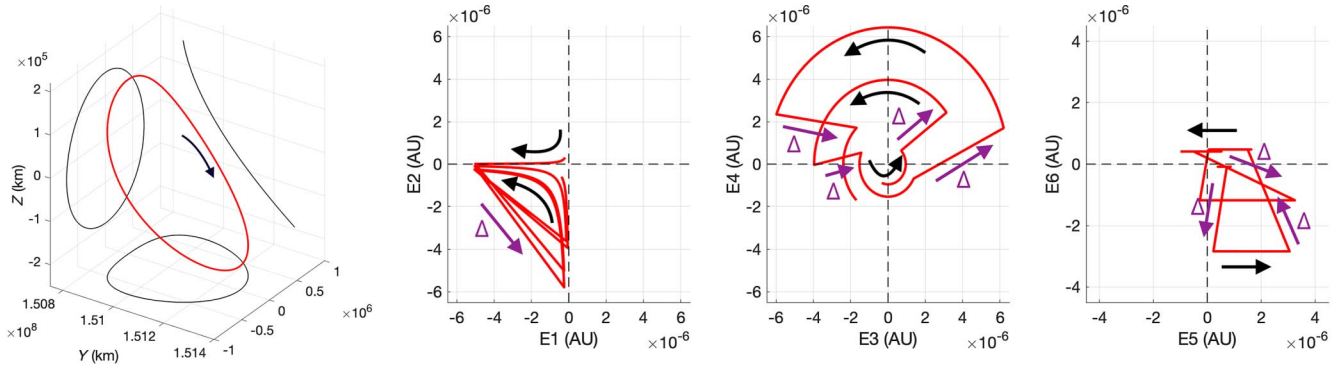

b) Evolution of the Floquet components for a trajectory close to a halo orbit with station-keeping maneuvers

Fig. 1 Comparison between trajectories with and without station-keeping maneuvers. Black arrows show the sense of orbital motion, and cyan arrows show the jumps associated to maneuvers.

epoch t, this deviation can be written in the local basis $\{\overline{\boldsymbol{e}}_i(t)\}$ defined by the Floquet modes as

$$\boldsymbol{\delta} = \sum_{i=1}^{6} c_i \overline{\boldsymbol{e}}_i(t) \tag{5}$$

We recall that $\overline{\boldsymbol{e}}_1(t)$ is the unstable direction, and we are interested in performing a maneuver that cancels the component c_1. Notice that we can write

$$\begin{aligned} c_1 &= \frac{\det(\boldsymbol{\delta}, \overline{\boldsymbol{e}}_2(t), \ldots, \overline{\boldsymbol{e}}_6(t))}{\det(\overline{\boldsymbol{e}}_1(t), \ldots, \overline{\boldsymbol{e}}_6(t))} = \pi_1^1(t)\delta x + \cdots + \pi_6^1(t)\delta\dot{z} \\ &= \langle \boldsymbol{\pi}^1(t), \boldsymbol{\delta}(t) \rangle \end{aligned} \tag{6}$$

where the components of $\boldsymbol{\pi}^1(t) = (\pi_1^1(t), \ldots, \pi_6^1(t))$ are the signed minors of the components of the first column of the matrix $(\boldsymbol{\delta}, \overline{\boldsymbol{e}}_2(t), \ldots, \overline{\boldsymbol{e}}_6(t))$ divided by the determinant of the Floquet basis. The components of $\boldsymbol{\pi}^1(t)$ are called the *projection factors* along the unstable direction. Notice that they do not depend on the error vector but only on the Floquet basis, so they need to be computed only once when the nominal orbit is selected. The computation of c_1 can be implemented in a very efficient way: at any time the unstable component along the unstable direction c_1 of the error vector $\boldsymbol{\delta} = (\delta x, \delta y, \delta z, \delta\dot{x}, \delta\dot{y}, \delta\dot{z})^T$ is just the dot product between the projection factor $\boldsymbol{\pi}^1(t)$ and $\boldsymbol{\delta}$.

Assume that $\Delta = (0, 0, 0, \Delta v_x, \Delta v_y, \Delta v_z)^T$ is the maneuver that is going to cancel the unstable component of $\boldsymbol{\delta}$. By definition, it verifies

$$\begin{aligned} \boldsymbol{\delta} + \Delta &= (\delta x, \delta y, \delta z, \delta\dot{x} + \Delta v_x, \delta\dot{y} + \Delta v_y, \delta\dot{z} + \Delta v_z)^T \\ &= \sum_{i=2}^{6} c_i \overline{\boldsymbol{e}}_i(t) \end{aligned}$$

It is easy to see that this implies that $\langle \boldsymbol{\pi}^1(t), \Delta \rangle = -c_1$; that is, the maneuver must satisfy

$$\pi_4^1(t)\Delta v_x + \pi_5^1(t)\Delta v_y + \pi_6^1(t)\Delta v_z = -c_1 \tag{7}$$

Accounting for this linear equation, the maneuver Δ can be determined by either imposing a constraint on the available directions of the control, or minimizing a suitable norm of the control vector. For instance, if we do not have any a priori restriction in the type of maneuvers to be performed, they can be selected in the straightforward way minimizing $\|\Delta\| = \sqrt{\Delta v_x^2 + \Delta v_y^2 + \Delta v_z^2}$. Then, the minimum-norm solution that satisfies Eq. (7) is given by

$$\begin{aligned} (\Delta v_x, \Delta v_y, \Delta v_z) = \Bigg(& \frac{-c_1\pi_4^1(t)}{\sqrt{\pi_4^1(t)^2 + \pi_5^1(t)^2 + \pi_6^1(t)^2}}, \\ & \frac{-c_1\pi_5^1(t)}{\sqrt{\pi_4^1(t)^2 + \pi_5^1(t)^2 + \pi_6^1(t)^2}}, \frac{-c_1\pi_6^1(t)}{\sqrt{\pi_4^1(t)^2 + \pi_5^1(t)^2 + \pi_6^1(t)^2}} \Bigg) \end{aligned} \tag{8}$$

In case we are required to thrust along a fixed direction, $\Delta = \gamma \boldsymbol{u}$, where $\boldsymbol{u} = (0, 0, 0, u_x, u_y, u_z)^T$ is a unitary vector, and $|\gamma| = \|\Delta\|$, then, using Eq. (7), we get

$$\gamma = \frac{-c_1}{\pi_4^1(t)u_x + \pi_5^1(t)u_y + \pi_6^1(t)u_z} \tag{9}$$

B. Velocity Constraint Approach

In the RLP frame, let $\boldsymbol{\xi} = (x, y, z, \dot{x}, \dot{y}, \dot{z})^T$ denote the state of the spacecraft where a station-keeping maneuver is required. The velocity constraint approach looks for a maneuver Δ such that the propagation of the state $\boldsymbol{\xi} + \Delta$ up to the third (or fourth) crossing with the $\{y = 0\}$ plane has the x component of the velocity vector, $\dot{x}$, equal to zero. We recall that, due to the symmetries of the CRTBP, LPOs, like

the Lypaunov, halo, quasi-halo, and Lissajous orbits, satisfy $\dot{x} = 0$ at the $\{y = 0\}$ plane crossing. Hence, this simple strategy ensures that the trajectory will continue librating about the equilibrium point.

There are different ways to find the required Δ that ensures the $\dot{x} = 0$ plane crossing constraint. The most common ones use differential corrector, and/or optimization methods in case a minimization is required. In this paper, we just use a differential corrector to find the required Δ. For completeness, let us briefly describe the differential corrector scheme used in the simulations.

We define the Poincaré map $\mathcal{P}$ as the map that, given an initial condition $\boldsymbol{\xi}$, returns the state of the spacecraft at the third (or fourth) crossing with the $\{y = 0\}$ plane, and denote $\mathcal{P}_{\dot{x}}(\boldsymbol{\xi})$ the x-velocity component of $\mathcal{P}(\boldsymbol{\xi})$. The x-axis velocity constraint at plane crossing requires the maneuver Δ be such that

$$\mathcal{P}_{\dot{x}}(\boldsymbol{\xi} + \Delta) = 0 \tag{10}$$

which reduces the problem to finding the zero of this function of Δ, which can be solved using a differential corrector scheme.

We use a Newton–Raphson method to solve Eq. (10) by iterating $\Delta_{i+1} = \Delta_i + \boldsymbol{h}$ and $\xi_{i+1} = \boldsymbol{\xi}_i + \Delta_{i+1}$, where $\boldsymbol{h} = (h_1, h_2, h_3)$ is the solution of the linear system

$$D\mathcal{P}_{\dot{x}}(\boldsymbol{\xi}_i)\boldsymbol{h} = -\mathcal{P}_{\dot{x}}(\boldsymbol{\xi}_i) \tag{11}$$

To solve the linear system, one can impose constraints on the equation, which is equivalent to constraining the thrust direction, or find the minimum-norm solution given by $\boldsymbol{h} = -D\mathcal{P}^T_{\dot{x}}(\boldsymbol{\xi}_i)(D\mathcal{P}_{\dot{x}}(\boldsymbol{\xi}_i)D\mathcal{P}^T_{\dot{x}}(\boldsymbol{\xi}_i))^{-1}\mathcal{P}(\boldsymbol{\xi}_i)$.

If $D\mathcal{P} = [dp_{i,j}]$ is the 6×6 matrix representing the differential of Poincaré map (it includes the trivial y row) and $D\mathcal{P}_{\dot{x}}$ is the fourth row in $D\mathcal{P}$, then Eq. (11) can be written as $dp_{44}h_1 + dp_{45}h_2 + dp_{46}h_3 = -\mathcal{P}_{\dot{x}}(\boldsymbol{\xi})$. The minimum-norm solution of Eq. (11) is given by

$$(h_1, h_2, h_3) = \left(-\frac{\mathcal{P}_{\dot{x}}(\boldsymbol{\xi})dp_{44}}{\sqrt{dp_{44}^2 + dp_{45}^2 + dp_{46}^2}}, -\frac{\mathcal{P}_{\dot{x}}(\boldsymbol{\xi})dp_{45}}{\sqrt{dp_{44}^2 + dp_{45}^2 + dp_{46}^2}}, -\frac{\mathcal{P}_{\dot{x}}(\boldsymbol{\xi})dp_{46}}{\sqrt{dp_{44}^2 + dp_{45}^2 + dp_{46}^2}} \right) \tag{12}$$

However, if we restrict the maneuver to be along a specific thrust direction, the unknown becomes the maneuver magnitude, and the linear equation (11) has only one unknown. For instance, if $\Delta = \gamma \boldsymbol{u}$, with $\boldsymbol{u} = (0, 0, 0, u_x, u_y, u_z)^T$ a unitary vector, Eq. (11) can be rewritten as

$$h = -\frac{\mathcal{P}_{\dot{x}}(\boldsymbol{\xi}_i)}{dp_{44}u_x + dp_{45}u_y + dp_{46}u_z} \tag{13}$$

and Eq. (10) is solved by iterating $\gamma_{i+1} = \gamma_i + h$, $\Delta_{i+1} = \gamma_{i+1}\boldsymbol{u}$, and $\boldsymbol{\xi}_{i+1} = \boldsymbol{\xi}_i + \Delta_{i+1}$.

IV. Jet Transport Implementation and Analysis

In the preceding section, we have made use of the Poincaré map to define the velocity constraint station-keeping procedure; later we are also going to use this map for the analysis of the station-keeping strategies. The *jet transport* (JT) method, which is not strictly needed for the implementation of our station-keeping strategies, provides high-order expansions of Poincaré maps, as well as a the possibility of making thousands of iterations of the map at a very reduced computational cost while keeping the same accuracy. So, it is a powerful tool for the analysis of the strategies; moreover, due to its simplicity in the representation of any function, it can also provide closed-form controllers that could be suitable to be implemented onboard. In this section, we briefly explain the basics and the ideas behind this method. More details about JT, its properties, and implementation can be found in [21,22].

A. Jet Transport Propagation

Jet transport is an automatic differentiation technique that allows obtaining high-order Taylor expansions of nonlinear functions and, in particular, of the image under the flow of ordinary differential equations (ODEs) of a set of initial conditions and a set of parameters.

If the ODE of the dynamic model is $\dot{\boldsymbol{x}} = f(\boldsymbol{x}, \boldsymbol{p}, t)$, where $\boldsymbol{x} \in \mathbb{R}^n$ are the state variables and $\boldsymbol{p} \in \mathbb{R}^m$ are the set of parameters, its flow with respect to the initial values $\boldsymbol{x}(t_0) = \boldsymbol{x}_0$ and $\boldsymbol{p} = \boldsymbol{p}_0$ is usually denoted by $\boldsymbol{x}(t) = \Phi(t; \boldsymbol{x}_0, \boldsymbol{p}_0, t_0)$. For given arbitrary deviations of the initial conditions, $[\boldsymbol{x}_0] = \boldsymbol{x}_0 + \delta\boldsymbol{x}_0$, and parameters $[\boldsymbol{p}_0] = \boldsymbol{p}_0 + \delta\boldsymbol{p}_0$, the JT procedure provides a Taylor expansion of $\Phi(t; \boldsymbol{x}_0 + \delta\boldsymbol{x}_0, \boldsymbol{p}_0 + \delta\boldsymbol{p}_0, t_0)$ at time t_f of the form

$$\begin{aligned}\Phi(t_f; \boldsymbol{x}_0 + \delta\boldsymbol{x}_0, \boldsymbol{p}_0 + \delta\boldsymbol{p}_0, t_0) &= \boldsymbol{x}_f + \mathcal{Q}^k_{t_f}(\delta\boldsymbol{x}_0, \delta\boldsymbol{p}_0) \\ &= \boldsymbol{x}_f + \sum_{1 \le k_1 + \cdots + k_n + \cdots + k_{n+m} \le k} \boldsymbol{c}_{k_1 \cdots k_{n+m}} \delta x_{0,1}^{k_1} \cdots \delta x_{0,n}^{k_n} \delta p_{0,1}^{k_{n+1}} \cdots \delta p_{0,m}^{k_{n+m}}\end{aligned} \tag{14}$$

where $\boldsymbol{x}_f = \Phi(t_f; \boldsymbol{x}_0, \boldsymbol{p}_0, t_0)$ is the nominal state at time t_f, $\delta\boldsymbol{x}_0 = [\delta x_{0,1}, \ldots, \delta x_{0,n}]^T$, $\delta\boldsymbol{p}_0 = [\delta p_{0,1}, \ldots, \delta p_{0,m}]^T$, $\mathcal{Q}^k_{t_f}$ is a polynomial of degree $k = k_1 + \cdots + k_n + \cdots + k_{n+m}$, and $\boldsymbol{c}_{k_1 \cdots k_{n+m}}$ are the coefficients of the polynomial. Note that, once the coefficients $\boldsymbol{c}_{k_1 \cdots k_{n+m}}$ have been determined, the computation of $\Phi(t_f; \boldsymbol{x}_0 + \delta\boldsymbol{x}_0, \boldsymbol{p}_0 + \delta\boldsymbol{p}_0, t_0)$, for any deviation of the initial conditions and parameters, only requires a polynomial evaluation, so it is very fast.

The accuracy of the expansions depends on the size of $\delta\boldsymbol{x}_0$ and $\delta\boldsymbol{p}_0$, as well as the total integration time interval $t_f - t_0$. Notice that in the station-keeping problem under consideration, we do not have parameters that vary. To check accuracy of the expansions, we have considered R-sets of perturbations of the form: $\boldsymbol{x}_0 + \delta\boldsymbol{x}_0 = (x_h + R\cos\theta, 0, z_h + R\cos\theta, 0, \dot{y}_h, 0)$, with $\theta \in [0, 2\pi]$, where $\boldsymbol{x}_0 = (x_h, 0, z_h, 0, \dot{y}_h, 0)$ is the initial condition of the halo orbit. For a fixed value of R, we have taken N perturbed initial conditions, which are numerically propagated up to $t = t_f$ and compared with the evaluation of the JT series at time t_f given by Eq. (14), using different orders k of the expansions. To measure the accuracy of the JT expansions, we define the error vector $\varepsilon^k = \boldsymbol{x}^n - \boldsymbol{x}^k = [\varepsilon_j^{k,x}, \varepsilon_j^{k,y}, \varepsilon_j^{k,z}, \varepsilon_j^{k,\dot{x}}, \varepsilon_j^{k,\dot{y}}, \varepsilon_j^{k,\dot{z}}]^T$, where $\boldsymbol{x}^n$ and $\boldsymbol{x}^k$ are the numerically propagated state vectors and their JT evaluation of order k, respectively. Then, the position and velocity error indicators are

$$\begin{aligned}\varepsilon^k_{\text{pos}} &= \frac{1}{N}\sum_{j=1}^{N} \sqrt{(\varepsilon_j^{k,x})^2 + (\varepsilon_j^{k,y})^2 + (\varepsilon_j^{k,z})^2}, \\ \varepsilon^k_{\text{vel}} &= \frac{1}{N}\sum_{j=1}^{N} \sqrt{(\varepsilon_j^{k,\dot{x}})^2 + (\varepsilon_j^{k,\dot{y}})^2 + (\varepsilon_j^{k,\dot{z}})^2}\end{aligned} \tag{15}$$

Estimates on how these expansions behave for a halo orbit with a z amplitude of 150,000 km, and for different time intervals and deviations from the initial conditions, are given in Table 1. The results given in this table show that series of at most order $k = 4$ are required to perform very accurate propagation in a large neighborhood of the halo orbit. Deviations of 10,000 km, which are much larger than the ones required for the station-keeping analysis, provide errors of order 10^{-4} km in position, and 10^{-8} m/s in velocity for time intervals of a quarter of the period of the halo orbit. Moreover, for deviations of the order of 100 km, the accuracy for one period time interval and order $k = 4$ is $[1.31 \times 10^2 \text{ km}, 2.61 \times 10^{-2} \text{ m/s}]$, which is really good considering that, for this halo orbit, the characteristic Floquet multiplier is of the order of 1500; this means that, the final differences between the two propagations are multiplied approximately by this factor, and so, the results after one period propagation are in practice three orders of magnitude smaller than the ones given in the table.

B. Poincaré Map Computations Using JT

Let $\boldsymbol{x}_0$ be a state on the nominal halo orbit at time t_0, $\delta\boldsymbol{x}_0$ be the deviation of the satellite relative to this nominal state, and Δ be a

Table 1 Accuracy of the JT with respect to a direct numerical integration for three different integration times t_f, and four different expansion orders k

t_f	R, km	$k = 1[\varepsilon^1_{\text{pos}}, \varepsilon^1_{\text{vel}}]$	$k = 2[\varepsilon^2_{\text{pos}}, \varepsilon^2_{\text{vel}}]$	$k = 3[\varepsilon^3_{\text{pos}}, \varepsilon^3_{\text{vel}}]$	$k = 4[\varepsilon^4_{\text{pos}}, \varepsilon^4_{\text{vel}}]$
$t_f = 1/4T^{\text{a}}$	10	$[3.58 \cdot 10^{-4}, 7.13 \cdot 10^{-8}]$	$[2.33 \cdot 10^{-5}, 4.64 \cdot 10^{-9}]$	$[2.33 \cdot 10^{-5}, 4.64 \cdot 10^{-9}]$	$[2.33 \cdot 10^{-5}, 4.64 \cdot 10^{-9}]$
	100	$[3.76 \cdot 10^{-2}, 7.48 \cdot 10^{-6}]$	$[2.43 \cdot 10^{-5}, 4.83 \cdot 10^{-9}]$	$[2.38 \cdot 10^{-5}, 4.73 \cdot 10^{-9}]$	$[2.38 \cdot 10^{-5}, 4.73 \cdot 10^{-9}]$
	1000	$[3.76, 7.48 \cdot 10^{-4}]$	$[2.17 \cdot 10^{-3}, 4.31 \cdot 10^{-7}]$	$[2.37 \cdot 10^{-5}, 4.72 \cdot 10^{-9}]$	$[2.25 \cdot 10^{-5}, 4.48 \cdot 10^{-9}]$
	10,000	$[3.76 \cdot 10^{2}, 7.48 \cdot 10^{-2}]$	$[2.16, 4.31 \cdot 10^{-4}]$	$[2.21 \cdot 10^{-2}, 4.40 \cdot 10^{-6}]$	$[1.93 \cdot 10^{-4}, 3.85 \cdot 10^{-8}]$
$t_f = 1/2T^{\text{a}}$	10	$[4.67 \cdot 10^{-2}, 9.29 \cdot 10^{-6}]$	$[1.70 \cdot 10^{-5}, 3.39 \cdot 10^{-9}]$	$[4.46 \cdot 10^{-6}, 8.88 \cdot 10^{-10}]$	$[4.47 \cdot 10^{-6}, 8.88 \cdot 10^{-10}]$
	100	$[4.67, 9.29 \cdot 10^{-4}]$	$[1.57 \cdot 10^{-2}, 3.13 \cdot 10^{-6}]$	$[6.56 \cdot 10^{-5}, 1.31 \cdot 10^{-8}]$	$[4.58 \cdot 10^{-6}, 9.12 \cdot 10^{-10}]$
	1000	$[4.67 \cdot 10^{2}, 9.30 \cdot 10^{-2}]$	$[1.57 \cdot 10^{1}, 3.13 \cdot 10^{-3}]$	$[6.75 \cdot 10^{-1}, 1.34 \cdot 10^{-4}]$	$[3.33 \cdot 10^{-2}, 6.64 \cdot 10^{-6}]$
	10,000	$[5.62 \cdot 10^{4}, 1.12 \cdot 10^{1}]$	$[2.07 \cdot 10^{4}, 4.12]$	$[9.58 \cdot 10^{3}, 1.91]$	$[5.03 \cdot 10^{3}, 1.00]$
$t_f = 1T^{\text{a}}$	10	$[9.99 \cdot 10^{1}, 1.99 \cdot 10^{-2}]$	$[1.90, 3.77 \cdot 10^{-4}]$	$[4.46 \cdot 10^{-2}, 8.89 \cdot 10^{-6}]$	$[1.20 \cdot 10^{-3}, 2.39 \cdot 10^{-7}]$
	100	$[1.05 \cdot 10^{4}, 2.08]$	$[2.03 \cdot 10^{3}, 4.04 \cdot 10^{-1}]$	$[4.85 \cdot 10^{2}, 9.65 \cdot 10^{-2}]$	$[1.31 \cdot 10^{2}, 2.61 \cdot 10^{-2}]$
	1000	$[1.34 \cdot 10^{8}, 2.68 \cdot 10^{4}]$	$[1.35 \cdot 10^{8}, 2.69 \cdot 10^{4}]$	$[1.36 \cdot 10^{8}, 2.71 \cdot 10^{4}]$	$[1.39 \cdot 10^{8}, 2.77 \cdot 10^{4}]$

The units of the position and velocity errors are km and m/s, respectively.
[a]T is the orbital period of the halo orbit.

maneuver performed at time t_0 (recall that the first three components of Δ are zero, and only the last three velocity components are undetermined parameters for Δ). We denote the set (jet) of initial conditions at the initial time t_0 as

$$[\boldsymbol{x}_0] = \boldsymbol{x}_0 + \delta\boldsymbol{x}_0 + \Delta$$

and its propagation up to time t_f, corresponding to the third intersection of $\boldsymbol{x}_0$ with the $\{y = 0\}$ plane, by

$$[\boldsymbol{x}_f] = \boldsymbol{x}_f + \mathcal{Q}^k_{\boldsymbol{x}_f}(\delta\boldsymbol{x}_0, \Delta) \tag{16}$$

Notice that $[\boldsymbol{x}_f]$ gives, by means of the order k polynomial $\mathcal{Q}^k_{\boldsymbol{x}_f}$, the propagation of any state in the neighborhood of $\boldsymbol{x}_0$ that is affected by a maneuver Δ up to the selected Poincaré section $\{y = 0\}$. Hence, in order to know the behavior of the Poincaré map for states close to $\boldsymbol{x}_0$, and affected by a maneuver Δ, we just need to evaluate the polynomial instead of propagating the whole trajectory again.

As a remark, observe that the Poincaré map is defined by the condition $\{y = 0\}$ and not as a fixed-time propagation. If t_f is the propagation time that $\boldsymbol{x}_0$ needs to reach $\{y = 0\}$, typically states in the vicinity of $\boldsymbol{x}_0$ need a slightly different amount of time and, consequently, the propagation time up to the Poincaré section is also a function of $\delta\boldsymbol{x}_0$ and Δ. Further details on how $\mathcal{Q}^k_{\boldsymbol{x}_f}$ is computed can be found in [22,37,38].

C. Floquet Mode Procedure Using JT

We recall that, given a state deviation $\delta\boldsymbol{x}_\mathbf{0}$ at time t_0, the projection on the unstable Floquet mode $\bar{\boldsymbol{e}}_1(t_0)$ is

$$c_1 = \langle \boldsymbol{\pi}^1(t_0), \delta\boldsymbol{x}_\mathbf{0} \rangle$$

where $\boldsymbol{\pi}^1(t_0) = (\pi^1_1(t_0), \pi^1_2(t_0), \pi^1_3(t_0), \pi^1_4(t_0), \pi^1_5(t_0), \pi^1_6(t_0))$ is the projection factor along the unstable direction. In the framework of the JT, the above equation is a polynomial equation in the variables $\delta\boldsymbol{x}_\mathbf{0}$ (in fact, it is a linear expression in this particular case), this is $c_1 = \mathcal{Q}^k_{c_1}(\delta\boldsymbol{x}_\mathbf{0})$. In this way, the Floquet mode control approach can be formulated as finding the maneuver $\Delta = (0, 0, 0, \Delta v_x, \Delta v_y, \Delta v_z)^T$ that cancels the unstable mode c_1:

$$\pi^1_4(t_0)\Delta v_x + \pi^1_5(t_0)\Delta v_y + \pi^1_6(t_0)\Delta v_z = -c_1$$

which is also a polynomial relation, now in the variables $\delta\boldsymbol{x}_\mathbf{0}$ and Δ. Assuming that the maneuvers are applied along a fixed direction defined by a unitary vector $\boldsymbol{u} = (0, 0, 0, u_x, u_y, u_z)$, that is, $\Delta = \gamma\boldsymbol{u}$, we get

$$\gamma = \frac{-c_1}{\pi^1_4(t_0)u_x + \pi^1_5(t_0)u_y + \pi^1_6(t_0)u_z}.$$

Now, γ is again formally a polynomial in the variables $\delta\boldsymbol{x}_\mathbf{0}$.

D. Floquet Mode Procedure Using JT at Time t_f

The above procedure can be easily modified requiring that the maneuver Δ cancels the unstable component at a certain final time t_f instead of at $t = t_0$. Using the jet given by Eq. (16), we can write the deviation with respect to the nominal state at $t = t_f$ as $\delta\boldsymbol{x}_f = \mathcal{Q}^k_{\boldsymbol{x}_f}(\delta\boldsymbol{x}_\mathbf{0}, \Delta)$. Then, if $\boldsymbol{\pi}^1(t_f)$ is the projection factor along the unstable direction at t_f, the unstable component $\bar{c}_1$ at this epoch is expressed as a polynomial function in the variables $\delta\boldsymbol{x}_\mathbf{0}$ and Δ:

$$\bar{c}_1 = \langle \boldsymbol{\pi}^1(t_f), \delta\boldsymbol{x}_\boldsymbol{f} \rangle = \mathcal{P}^k_{\bar{c}_1}(\delta\boldsymbol{x}_\mathbf{0}, \Delta)$$

Assuming the fixed direction constraint $\Delta = \gamma\boldsymbol{u}$, we obtain the implicit equation $\mathcal{P}^k_{\bar{c}_1}(\delta\boldsymbol{x}_\mathbf{0}, \gamma\boldsymbol{u}) = \bar{c}_1$, which easily gives γ as a polynomial in $\delta\boldsymbol{x}_\mathbf{0}$. It is worth mentioning here that, unlike the velocity constraint controller that needs to consider a propagation until the intersection with the $\{y = 0\}$ plane, the Floquet mode controller can be implemented without this restriction and, moreover, for any arbitrary time $t_f \geq t_0$.

E. Velocity Constraint Procedure Using JT

As it was explained in Sec. III.B, the velocity constraint procedure consists in finding Δ such that $\dot{x} = 0$ at a certain $\{y = 0\}$ plane crossing (usually the third or the fourth). Denoting by $[\dot{x}_f]$ the $\dot{x}$ component of $[\boldsymbol{x}_f]$ given in Eq. (16), to implement the procedure we need to solve the implicit equation

$$[\dot{x}_f] = \mathcal{Q}^k_{\dot{x}_f}(\delta\boldsymbol{x}_0, \Delta) = 0 \tag{17}$$

providing Δ in terms of $\delta\boldsymbol{x}_0$. As in the previous cases, Eq. (17) is underdetermined (one equation and three unknowns for Δ). Assuming again the fixed direction condition for the maneuvers, $\Delta = \gamma\boldsymbol{u}$, the equation can be solved using, for instance, a Newton–Raphson method. Then, the solution is formally written as

$$\gamma = \mathcal{P}^k_{\dot{x}_f}(\delta\boldsymbol{x}_0) \tag{18}$$

which is again a k-order polynomial expansion that explicitly provides the control maneuver as a function of $\delta\boldsymbol{x}_0$.

V. Analyses on the Two Station-Keeping Strategies

In this section, we compare the Floquet mode approach and the velocity constraint at plane-crossing procedure in order to clarify the differences and similarities between the two from a dynamic point of view. Section V.A describes the behavior of the strategies by projecting the trajectory of the spacecraft in the Floquet mode reference system, which allows understanding the geometry of the two methods. Section V.B uses the Poincaré maps provided by the JT procedure for each strategy and compares the controllers from an analytic point of view. Finally, Secs. V.C and V.D are devoted to the study of the stability and long-term behavior of both procedures.

A. Dynamics of Station-Keeping

To better understand the differences between the station-keeping strategies described in Sec. III, we have analyzed the behavior of the Δ maneuvers in the Floquet reference frame. As previously discussed, this is a useful tool to understand the geometry of each station-keeping method, and it also allows the comparison between different procedures. As a reference example, a halo orbit with 150,000 km of z amplitude, which is close to RST's orbit, has been considered as the nominal orbit [16]. This nominal orbit $\boldsymbol{x}(t)$ and the associated Floquet modes $\{\overline{\boldsymbol{e}}_i(t)\}$ have been computed, and since all these functions are T-periodic, being T the halo orbit period, they are stored by means of their Fourier series for a fast retrieval at any time. For a given state of the satellite $\tilde{\boldsymbol{x}}(t)$ at a certain epoch t, we define an associated *nominal point* as the point of the nominal orbit $\boldsymbol{x}(t)$ isochronous with the spacecraft.

We start with the satellite located close to the reference orbit and propagate it for five orbital periods, applying routine station-keeping maneuvers using either the Floquet mode approach (FM; see Sec. III.A) or the velocity constraint method (VX0; see Sec. III.B). The displaced initial condition is generated by introducing a random error, in both position and velocity, of order 10^{-6} in dimensionless units, which corresponds to 150 km error in position and 3 cm/s error in velocity. For both simulations the routine station-keeping maneuvers are performed each time the perturbed trajectory is at a distance of 5×10^{-6} DU ($\approx$750 km) along the unstable direction from the nominal point. This results in maneuvers approximately every 150 days. Finally, a 5 % error is applied in the modulus of the maneuver each time a maneuver is executed, but no errors on the maneuver direction are considered.

Figure 2 shows the trajectory of the satellite using the Floquet mode (Fig. 2a) and the velocity constraint procedure (Fig. 2b). In both cases, in addition to the classical xyz projection of the trajectory, projections on the plane generated by the stable and unstable modes $\{\overline{\boldsymbol{e}}_1(t), \overline{\boldsymbol{e}}_2(t)\}$ (saddle plane from now on), and the center and neutral components ($\{\overline{\boldsymbol{e}}_3(t), \overline{\boldsymbol{e}}_4(t)\}$ and $\{\overline{\boldsymbol{e}}_5(t), \overline{\boldsymbol{e}}_6(t)\}$, respectively) are given. Notice that each jump in the plots corresponds to a Δ maneuver that can be clearly appreciated in these three reference planes.

The projection of both controlled trajectories on the saddle plane shows clear similarities. Even if it is not required by the velocity constraint strategy, the maneuvers introduce jumps on the trajectory that cancel the unstable component, as it can be seen in Fig. 2b (top right). This makes sense, as the natural way to get close to a periodic orbit (with $\dot{x} = 0$ at the $\{y = 0\}$ plane intersection) is jumping on (or getting closer to) the orbits of the center-stable manifold, that is, canceling the unstable component. However, there are different ways to cancel this unstable component, and this makes the difference between the station-keeping procedures.

On the other hand, the projection of the trajectory on the center plane $\{\overline{\boldsymbol{e}}_3(t), \overline{\boldsymbol{e}}_4(t)\}$ shows a sequence of rotations along the center of the plot. Note that each time a maneuver is performed, the distance to the center changes. As neither of the station-keeping approaches imposes any requirement on this projection, one could have an unbounded growth of this distance. However, this has not been observed in the simulations. Finally, the projection on the neutral plane $\{\overline{\boldsymbol{e}}_5(t), \overline{\boldsymbol{e}}_6(t)\}$ accounts for the drift along the family of orbits, or drift in the orbital period, which is very small in both cases.

Finally, the left-hand side of Fig. 3 shows the magnitude of each of the nine Δ maneuvers required by the two station-keeping methods. The blue line corresponds to the FM station-keeping, whereas the red line corresponds to the VX0 station-keeping. Notice that the magnitudes of both Δ are very close, and that in most of the cases the FM has the smallest maneuvers.

From the above results, it seems that both strategies are performing almost the same (canceling the unstable mode) even though each approach uses a different algorithm. The only difference between the two methods is the direction in which each procedure chooses to cancel the instability. To better understand this fact we performed the same simulations but forcing the Δ maneuver to be in the same direction in both procedures, using Eq. (9) to find the magnitude in the FM case and Eq. (13) to solve the differential corrector in the VX0 case. The right-hand side of Fig. 3 shows the magnitude of the maneuvers if we force the station-keeping maneuvers along $\boldsymbol{u} = (0, 0, 0, 1, 0, 0)$ direction, which is close to thrusting along the sun–satellite line. Notice that in this case the magnitude of the maneuvers for both procedures is the same.

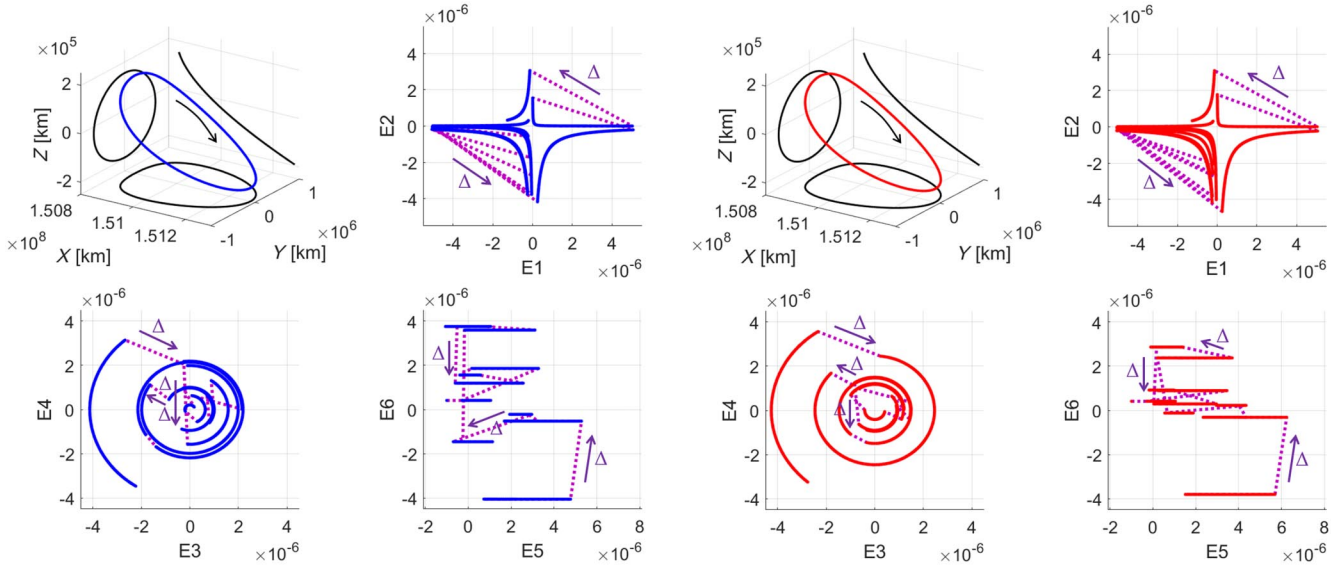

a) Floquet Mode station-keeping approach b) Velocity constraint station-keeping approach

Fig. 2 Trajectory of the satellite around a halo orbit after applying station-keeping maneuvers for five orbital periods in the RLP and Floquet mode reference frames.

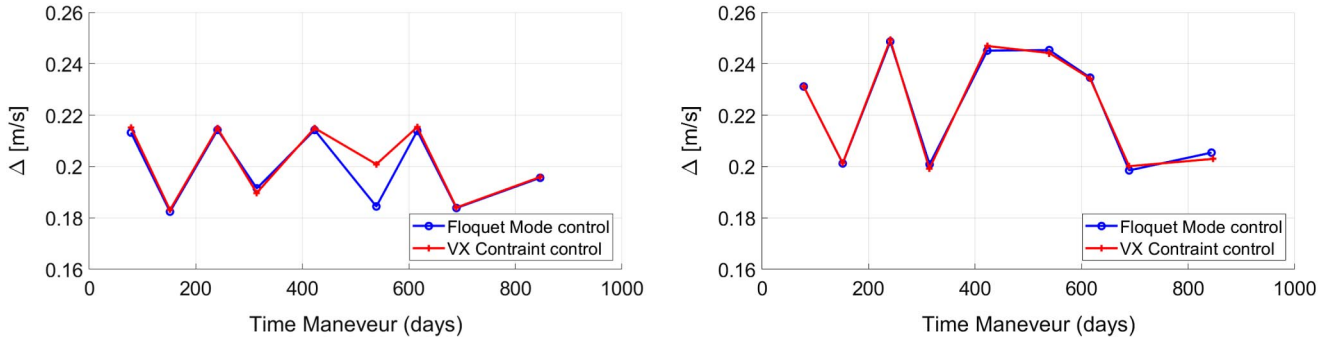

a) Δ maneuver with no constraint in the direction

b) Δ maneuver constrained to $u = (0, 0, 0, 1, 0, 0)^T$

Fig. 3 Magnitude of the individual Δ maneuvers over time for the Floquet mode (blue) and the velocity constraint (red) station-keeping strategies.

A natural question is to see how different directions affect the cost of the station-keeping, and if there is a maneuver direction that minimizes each of the individual maneuvers. Previous analysis from ARTEMIS [14] and WIND [12] suggests that the thrust direction that provides the minimum Δ cost is given by the position components of the stable eigendirection, but no demonstration to this fact is shown. In Sec. VI, we will study in more detail the relations between the thrust direction and the magnitude of the maneuvers.

B. Poincaré Map Analysis of the Controllers

To study the behavior of the station-keeping methods already discussed, we have performed long time simulations, involving several revolutions of the spacecraft along a periodic halo orbit, that characterize their stability properties. For these simulations, as is schematically explained in Fig. 4, we perform station-keeping maneuvers each time the spacecraft intersects the $\{z = 0\}$ or the $\{y = 0\}$ planes, and we compute the propagation from one intersection to the next by means of a Poincaré map using the JT procedure explained in Sec. IV.B. In this way, and defining the surface of section $\mathcal{N} = \{y = 0, z > 0\}$, we consider the Poincaré return map after one complete revolution

$$\mathcal{P}: \mathcal{N} \to \mathcal{N}$$

as the composition of four maneuvers ($\mathcal{M}_*$) and four Poincaré maps ($\mathcal{P}_*$); that is,

$$\mathcal{P} = \mathcal{P}_N \circ \mathcal{M}_W \circ \mathcal{P}_W \circ \mathcal{M}_S \circ \mathcal{P}_S \circ \mathcal{M}_E \circ \mathcal{P}_E \circ \mathcal{M}_N$$

If $\boldsymbol{x}^N \in \mathcal{N}$ is the initial nominal state on the halo orbit, and $\delta\boldsymbol{x}$ the actual deviation of the spacecraft with respect to it, then $\mathcal{M}_N(\boldsymbol{x}^N + \delta\boldsymbol{x})$ is the result of the first station-keeping the maneuver (computed by any of the controllers). This new state is propagated by $\mathcal{P}_E$ until the section $E = \{z = 0, y > 0\}$, where the second maneuver $\mathcal{M}_E$ is applied; then the Poincaré map $\mathcal{P}_S$ takes this state up to $\mathcal{S} = \{y = 0, z < 0\}$, where the maneuver $\mathcal{M}_S$ is performed. The procedure is repeated until the initial section $\mathcal{N}$ is reached again.

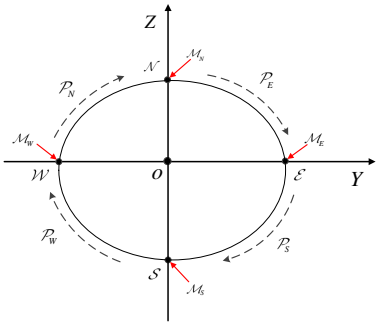

Fig. 4 Scheme of maneuvers and Poincaré maps along a halo orbit, which is traveled clockwise in the yz projection displayed.

We note that, by means of the JT technique, the maps $\mathcal{M}_*$ and $\mathcal{P}_*$ are represented by high-order formal expansions, and the computation of their composition, which is fast and accurate, gives $\mathcal{P}$. For a given station-keeping strategy, the stability of the map $\mathcal{P}$ characterizes the stability of the controller. Of course, there are other choices for the map $\mathcal{P}$, for instance, with more or less maneuvers per revolution; however, the final results remain essentially the same. The choice that has taken for $\mathcal{P}$, with four maneuvers per revolution, is simple and, moreover, is close to the actual number of maneuvers per revolution in real libration point missions.

We have considered the three station-keeping approaches given in Sec. IV.B: $\dot{x} = 0$ (VX0), Floquet mode at $t = 0$ (FM0), and Floquet mode at $t = t_f$ (FMf). We denote their corresponding $\mathcal{P}$ maps as $\mathcal{P}_{\dot{X}0}$, $\mathcal{P}_{F0}$, and $\mathcal{P}_{Ff}$, respectively. As we have mentioned before, thanks to the JT approach, we can obtain a nonlinear expansion of these maps, which are summarized in the Appendix. One can see that all three maps are almost the same up to first order; moreover, $\mathcal{P}_{\dot{X}0}$ and $\mathcal{P}_{Ff}$ are very similar even at degree 2. A statistical summary of the comparison is provided in Table 2.

C. Stability of the Controllers

The eigenvalues of the linear part of the three Poincaré maps defined in the previous section characterize the stability and geometrical behavior of the three station-keeping procedures. They are given in Table 3, to which we have added the eigenvalues of $\mathcal{P}_0 = \mathcal{P}_N \circ \mathcal{P}_W \circ \mathcal{P}_S \circ \mathcal{P}_E$, that is, the composition of the four Poincaré propagation without any intermediate maneuver.

The high instability of the halo orbit is displayed by the eigenvalue $\lambda_1 = 1636.9$ of the $\mathcal{P}_0$ map, which is driven to zero by any of the three controllers. This is because the station-keeping maneuvers are designed to cancel the instability of the periodic orbit by zeroing the unstable eigenvalue. It is interesting to note that the other eigenvalues, stable (λ_2), central ($\omega_{1,2,3}$), related to the eigenvalues of the monodromy matrix of the halo orbit λ_3 and $\bar{\lambda}_4$, and the tangent to the family of halo orbits λ_5, remain the same for all the maps. This means that the controllers do not ensure asymptotic stability; hence, in general, the spacecraft will be oscillating about the nominal halo orbit. To force it to tend toward the nominal orbit it would be necessary to apply other strategies, involving two or more linked maneuvers (for instance, a departure/insertion pair of maneuvers to insert into the orbit or into its stable manifold).

D. Long-Term Behavior of the Station-Keeping Strategies

We have analyzed the long-term behavior of the station-keeping strategies by iterating their associated Poincaré map for 1, 10, 100, and 1000 iterates. Taking into account that the period of a halo orbit is approximately half a year, these iterates roughly correspond to 6 months and 5, 50, and 500 years, respectively. As we have already seen, all three controllers are very similar; hence, their long-term qualitative behavior will also be similar. For this reason, we only present the results for $\mathcal{P}_{\dot{X}0}$.

Table 2 Maximum, minimum, and average differences between the 1st- and 2nd-order coefficients of the Poincaré maps

	$\mathcal{P}_{Ff}-\mathcal{P}_{F0}$			$\mathcal{P}_{\dot{X}0}-\mathcal{P}_{F0}$			$\mathcal{P}_{\dot{X}0}-\mathcal{P}_{Ff}$		
N	min	max	ave	min	max	ave	min	max	ave
1	1.536e − 11	8.430e − 7	1.130e − 7	3.366e − 8	0.001921	0.00030	3.365e − 8	0.001920	0.0002924
2	0.0144947	2.49672	0.8421	0.0144996	2.49746	0.842208	2.024e − 7	0.039417	0.0015351

The relative differences have been calculated as $\frac{\mathcal{P}_{Ff}-\mathcal{P}_{F0}}{\mathcal{P}_{F0}}$, $\frac{\mathcal{P}_{\dot{X}0}-\mathcal{P}_{F0}}{\mathcal{P}_{F0}}$, and $\frac{\mathcal{P}_{\dot{X}0}-\mathcal{P}_{Ff}}{\mathcal{P}_{Ff}}$.

Table 3 Eigenvalues of the linear parts of the Poincaré maps $\mathcal{P}_0$, $\mathcal{P}_{\dot{X}0}$, $\mathcal{P}_{F0}$, and $\mathcal{P}_{Ff}$

$\mathcal{P}$-map	λ_1	λ_2	$\omega_{1,2}$	ω_3
$\mathcal{P}_0$	1636.9064	0.0006	$0.9940 \pm 0.1093i$	1
$\mathcal{P}_{\dot{X}0}$	-1.047×10^{-16}	0.0006	$0.9940 \pm 0.1093i$	1
$\mathcal{P}_{F0}$	2.954×10^{-16}	0.0006	$0.9940 \pm 0.1093i$	1
$\mathcal{P}_{Ff}$	-4.175×10^{-16}	0.0006	$0.9940 \pm 0.1093i$	1

As in Sec. IV, we take initial conditions in the set C_R defined by

$$C_R = \boldsymbol{x}_0 + \delta\boldsymbol{x}_0 = \{(x_h + R\cos\theta, 0, z_h + R\cos\theta, 0, \dot{y}_h, 0), \theta \in [0, 2\pi]\}$$

where $\boldsymbol{x}_0 = (x_h, 0, z_h, 0, \dot{y}_h, 0)$ are the initial conditions of the halo orbit used in all the above computations. Figure 5 shows the images of C_R for $R = 10, 100, 1000$, and 10,000 km. The blue circle in each plot corresponds to the initial conditions set C_R, and the other curves are its images after 1 (red), 10 (yellow), 100 (purple), and 1000 (green) iterations. From this figure, it clearly follows that the long-term behavior is stable. Only for initial conditions with deviations $R = 10{,}000$ km present some divergence after 1000 iterations (500 years).

Furthermore, it happens that for a given deviation from the nominal state, we can distinguish between the first maneuver and the remaining ones. The first one, which is performed at $\mathcal{N}$, cancels the unstable component, whereas the others just prevent this component from growing. This general behavior is illustrated in Fig. 6, where we plot the trajectories, using the Floquet modes reference frame, for the different iterates. After the first maneuver, the controller enters into a steady regime where the unstable mode component $\boldsymbol{e}_1$ is close to zero (as it is also the stable one, $\boldsymbol{e}_2$), the neutral modes $\boldsymbol{e}_5$ and $\boldsymbol{e}_6$ are on a line, while the rotational ones $\boldsymbol{e}_3$ and $\boldsymbol{e}_4$ are on a circle. This fact is also present in Fig. 5, where we see that the first iterate "shrinks" the x amplitude while maintaining the z one, and this is because the unstable component of the orbit is always contained in the xy plane, having no out-of-plane component.

The cancellation of the unstable component at the first maneuver produces the reduction of the $\boldsymbol{e}_1$ component of the first iterate (in case the unstable component of the deviation were not zero), and after this, the iterates of the map enter into a steady regime. It is clear that this behavior has also a consequence on the cost of the maneuvers. The cost of the first maneuver is basically proportional to the $\boldsymbol{e}_1$ value of the initial unstable mode, which in the case of our C_R initial conditions is of the order of $4.6 \times 10^{-4} R$ m/s when the

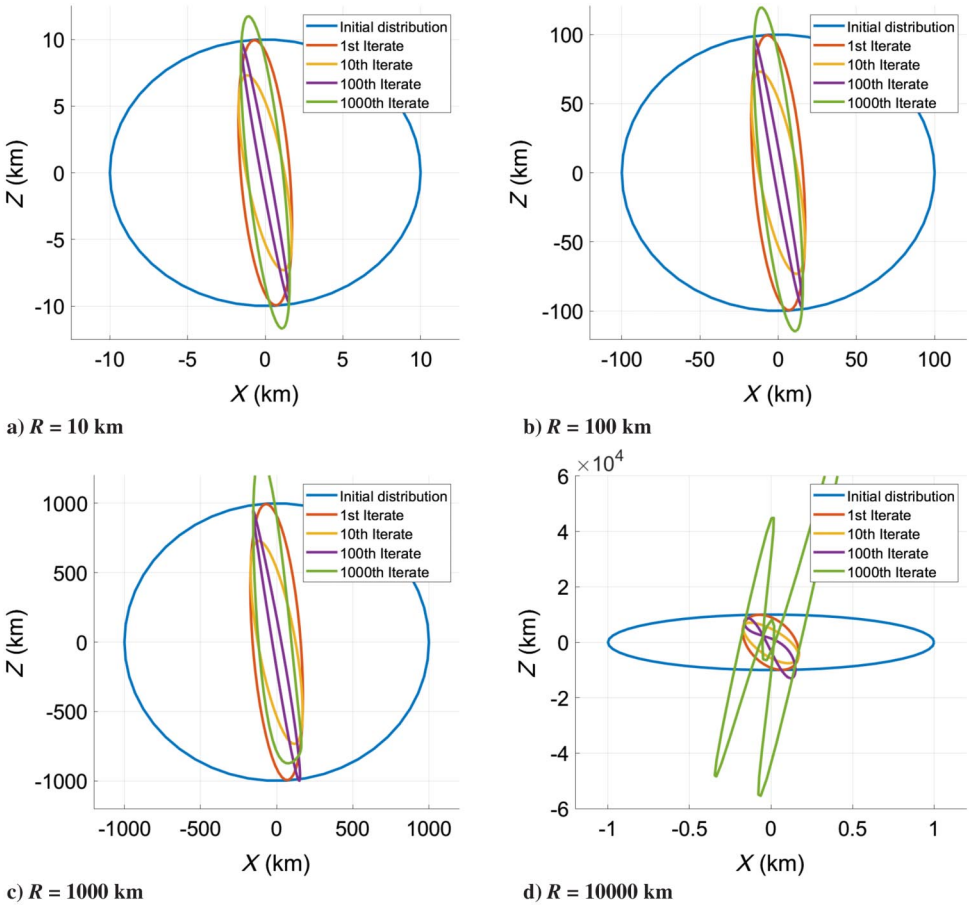

Fig. 5 Poincaré map iterates of initial conditions of the set C_R under the map $\mathcal{P}_{\dot{X}0}$.

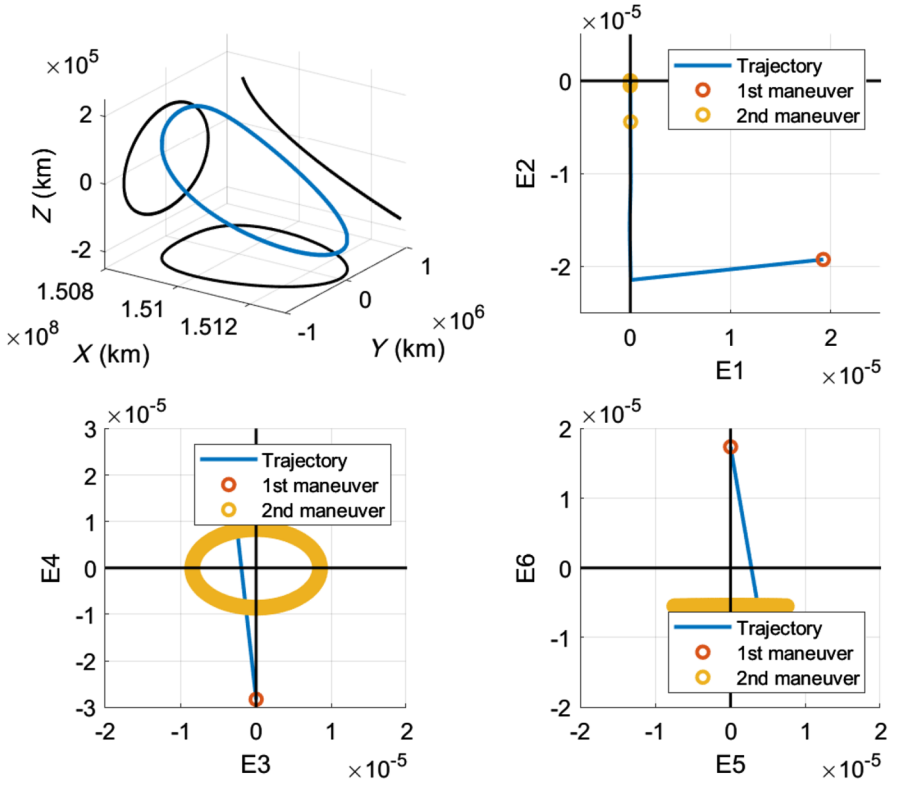

Fig. 6 Floquet mode decomposition for 1000 iterates of $\mathcal{P}_{\dot{X}0}$. Note that the initial state error is $\delta x = [1000\ \text{km}, 0\ \text{km}, 0\ \text{km}, 0\ \text{m/s}, 0\ \text{m/s}, 0\ \text{m/s}]$.

initial deviation R is measured in kilometers. While the cost of the steady regime also depends on the deviation with respect to the nominal orbit and it is almost negligible in all cases, ranging from an accumulated Δv of 2.2×10^{-7} m/s per year when $R = 10$ km, to 1.4×10^{-4} m/s per year when $R = 10{,}000$ km. Of course, this is a theoretical analysis of the controllers in their "pure state"; in practice, the state of the spacecraft is affected by errors in orbit determination, as well as maneuver execution errors. Hence, all the maneuvers cancel a small but nonnegligible estimated $\boldsymbol{e}_1$ component.

VI. Analyses on the Optimality of the Maneuver Directions

Let us now focus on finding the optimal thrust direction for station-keeping. As we have seen in the previous sections, the Δ is related to the jump the spacecraft has to do in the saddle plane in order to cancel the unstable component. Hence, there are two parameters that drive the size of Δ: the thrust direction, which defines the direction of the jump, and the distance between the spacecraft and the stable direction.

Previous studies [12,14,15] suggest that the minimum thrust direction is aligned with the position components of the stable direction. In this section, we analyze the size of the Δ as a function of the thrust direction, and find an analytical way to define the direction with the smallest magnitude. We also describe how looking at things on the saddle plane can help us to quantify how the constraints on the thrust direction can affect the overall Δv cost and define strategies to minimize this effect. Notice that all the results presented in this section have been done using the VX0 approach fixing the thrust direction [Eq. (13) in Sec. III.B] to find the station-keeping maneuvers. However, from the analysis in Sec. V.B, the same results apply for the FM approach.

A. Effect of Changes in the Maneuver Direction

To check the relation between the Δ magnitude and the jump on the saddle plane, we have performed the following simulations. We take an initial condition on the halo orbit displacing its location 10^{-6} DU ($\approx$150 km) along the unstable direction [i.e., its position in the Floquet mode basis is $\boldsymbol{s} = (\pm 10^{-6}, 0, 0, 0, 0, 0)^T$]. Then, for a set of different thrust directions, the station-keeping maneuver determined by the VX0 strategy along that thrust direction is applied. Given that the stable and unstable directions have a small z component when compared to the (x, y) component, to simplify the analysis, we have taken thrust directions in the xy plane $\boldsymbol{u} = (0, 0, 0, \cos\theta, \sin\theta, 0)^T$, with $\theta \in [-180 \quad 180]^\circ$.

The left-hand side of Fig. 7 shows the projection of different thrust directions in the RLP xy plane (i.e., the x, y velocity components of $\boldsymbol{u}$) together with the (x, y)-position components of the stable (e_{2x}, e_{2y}) (green) and unstable (e_{1x}, e_{1y}) (red) directions, where $\overline{\boldsymbol{e}}_1(t) = (e_{1x}, e_{1y}, e_{1z}, e_{1vx}, e_{1vy}, e_{1vz})$ and $\overline{\boldsymbol{e}}_2(t) = (e_{2x}, e_{2y}, e_{2z}, e_{2vx}, e_{2vy}, e_{2vz})$ are the unstable and stable Floquet modes at the nominal orbit isochronous point. On the right-hand side of Fig. 8, we have the projection of $\boldsymbol{u}$ on the saddle plane $\{\overline{\boldsymbol{e}}_1, \overline{\boldsymbol{e}}_2\}$. The colorcode in both plots is used to relate the thrust vector with the same angle θ.

Figure 8 shows the relation between the magnitude of Δ and the jump on the saddle plane. For each subplot, the two left plots show the projection on the saddle plane of the Δ found by the velocity constraint strategy. Note how, depending on the initial location on the saddle plane ($c_1 = +10^{-6}$ or $c_1 = -10^{-6}$), there is only a set of directions that allow one to control the spacecraft, and that in all cases Δ cancels the unstable mode (i.e., produces a jump in velocities such that $c_1 = 0$). Finally, the two right plots in Fig. 8 show the relation between the angle θ, which parameterizes the set of directions, and the Δ magnitude. The red and green vertical lines correspond to the θ values of the (x, y) components of the unstable and stable directions, respectively. We can see that the maneuver directions with smaller magnitudes correspond to those directions whose projection on the saddle plane is close to $(\pm 1, 0)$. On the other hand, we can see how the largest maneuver magnitudes are close to the $\{x - y\}$-position components of the unstable direction (red dotted line on right plots), whereas the smaller maneuvers are close to the $\{x - y\}$-position components of the stable one (green dotted line on the right plots).

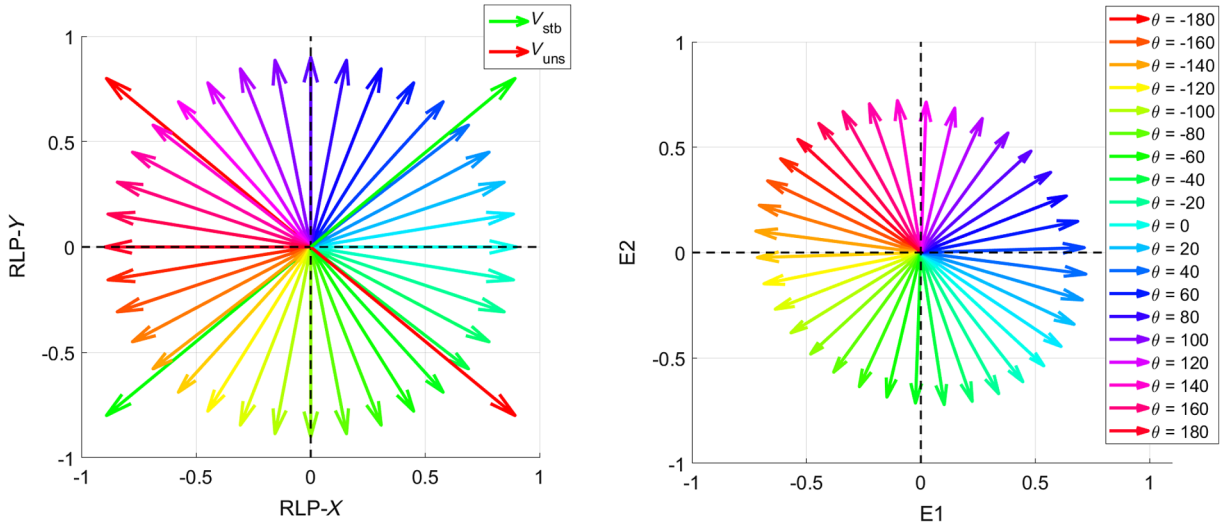

a) Projection of the velocity components of u on the xy-RLP plane

b) Projection of the velocity components of u on the saddle plane

Fig. 7 Projections of the thrust vector u, colorcoded to identify between plots the same values of the angle θ used to parameterize the thrust directions.

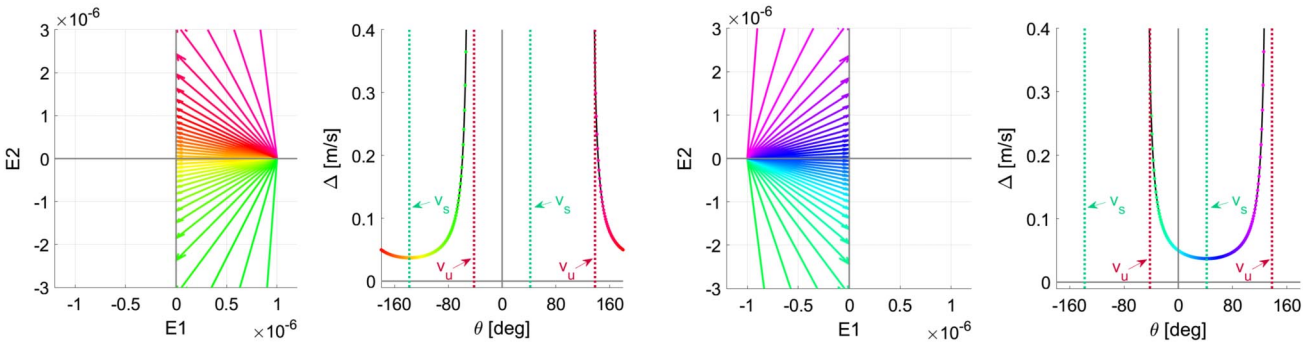

a) Initial condition on saddle plane at $(c_1, c_2) = (+10^{-6}, 0)$

b) Initial condition on saddle plane at $(c_1, c_2) = (-10^{-6}, 0)$

Fig. 8 Relation between the maneuver magnitude and the jump on the saddle plane. Left: Projection of Δ on the saddle plane. Right: Δ magnitude as a function of the $\theta = \arctan(\Delta v_y / \Delta v_x)$.

B. Determination of the Minimum-Cost Maneuver

As we have just seen, there is a relation between the jump on the unstable mode and the magnitude of Δ. We consider this fact looking forward to find an analytic expression for the minimum cost maneuver. For this purpose, we try to find the direction that gives the maximum variation on the unstable mode and the directions that do not introduce any variation on the unstable mode. It is reasonable to think that these two directions will be related with the bounds of the minimum and maximum $\Delta \boldsymbol{v}$ magnitudes, respectively.

Let $\boldsymbol{x}_0(t)$ be a point close to the halo orbit at time t, $\boldsymbol{\delta}_0(t)$ be the distance between the spacecraft and the isochronous point along the nominal halo orbit, and Δ be the maneuver to be applied. Recall Eq. (6), which gives us the deviation c_1 along the unstable mode at any time t. Hence, if $\boldsymbol{x}_0(t) + \Delta$ is the spacecraft state after the maneuver, we have that the difference along the unstable mode is given by

$$\Delta c_1 = \langle \boldsymbol{\pi}^1(t), \boldsymbol{\delta}_0(t) + \Delta \rangle - \langle \boldsymbol{\pi}^1(t), \boldsymbol{\delta}_0(t) \rangle = \langle \boldsymbol{\pi}^1(t), \Delta \rangle \tag{19}$$

To find an optimal Δ, we are interested in maximizing Δc_1. Note that the directions that maximize Δc_1 are such that small variations in the velocity component produce maximum changes in the unstable mode; hence a minimum Δ has to be close to these directions. Notice also that those directions such that $\Delta c_1 = 0$ have no effect on the unstable mode and cannot be used for station-keeping or require the largest Δ. To find these particular Δ directions, we need to find a relation between Δc_1 and the nonzero components of $\Delta = (0, 0, 0, \Delta v_x, \Delta v_y, \Delta v_z)$:

$$\Delta c_1 = \langle \boldsymbol{\pi}^1(t), \Delta \rangle = \pi_4^1(t)\Delta v_x + \pi_5^1(t)\Delta v_y + \pi_6^1(t)\Delta v_z \tag{20}$$

According to this last equation, there is a plane of directions of Δ such that $\Delta c_1 = 0$. Constraining the maneuver to be in the xy plane ($\Delta v_z = 0$), we get the unitary vectors that satisfy Eq. (20):

$$\Delta_0 = \left(0, 0, 0, \pm \frac{\pi_5^1(t)}{\sqrt{\pi_4^1(t)^2 + \pi_5^1(t)^2}}, \mp \frac{\pi_4^1(t)}{\sqrt{\pi_4^1(t)^2 + \pi_5^1(t)^2}}, 0\right) \tag{21}$$

To find the unitary vector Δ that maximizes $|\Delta c_1|$, we use Lagrange multipliers. Note that the problem can be stated as finding the extremum of the function $f(x, y, z) = \pi_4^1(t)x + \pi_5^1(t)y + \pi_6^1(t)z$ constrained to $g(x, y, z) = x^2 + y^2 + z^2 = 1$. The unitary Δ that maximizes $|\Delta c_1|$ are given by

$$\Delta_1 = \left(0, 0, 0, \pm \frac{\pi_4^1(t)}{\sqrt{\pi_4^1(t)^2 + \pi_5^1(t)^2 + \pi_6^1(t)^2}}, \right.$$
$$\left. \pm \frac{\pi_5^1(t)}{\sqrt{\pi_4^1(t)^2 + \pi_5^1(t)^2 + \pi_6^1(t)^2}}, \pm \frac{\pi_6^1(t)}{\sqrt{\pi_4^1(t)^2 + \pi_5^1(t)^2 + \pi_6^1(t)^2}}\right) \tag{22}$$

which is the same direction provided by the Floquet mode approach in Eq. (8). Clearly $\Delta_0 \perp \Delta_1$. Moreover, in case of further restrictions on the Δ direction, these can be easily considered for the determination of Δ. For instance, the maximum restricted to $z = 0$ is given by

$$\Delta_2 = \left(0, 0, 0, \pm \frac{\pi_4^1(t)}{\sqrt{\pi_4^1(t)^2 + \pi_5^1(t)^2}}, \pm \frac{\pi_5^1(t)}{\sqrt{\pi_4^1(t)^2 + \pi_5^1(t)^2}}, 0\right) \tag{23}$$

To check that maneuvers in the Δ_0 and Δ_1 directions behave as expected, we have performed the following simulations. Take an initial condition on the periodic orbit $\boldsymbol{x}_0(t)$, apply a $\Delta\boldsymbol{v}$ maneuver in one of these directions, and propagate the trajectory for 0.5 units of time (UT). The magnitude of the maneuvers applied is 10^{-4} DU/TU ($\approx$2.98 m/s). For comparison, aside from Δ_0 and Δ_1, we have also applied maneuvers in the ecliptic plane (i.e., $\Delta = (0, 0, 0, \cos\theta, \sin\theta, 0)$, with $\theta \in [-180 \quad 180]°$). Figure 9 depicts the results of these simulations.

On the top-left plot of Fig. 9, we show the projection on the (x, y) plane of the different Δ in relation to the position components of the stable (green) and unstable (red) eigendirections. The colored arrows correspond to different values of θ, the dashed black arrow corresponds to Δ_1, and the solid black arrow corresponds to Δ_0. Notice that Δ_1 is close to the stable eigenvector, and Δ_0 is close to the unstable one. On the top-right plot of Fig. 9, we show the projection of these directions on the saddle plane $\{\overline{\boldsymbol{e}}_1, \overline{\boldsymbol{e}}_2\}$, and we can see that the projection of Δ_0 is (0, 1) and cannot introduce any change in the $\overline{\boldsymbol{e}}_1$, as expected, whereas Δ_1 is close to (1, 0). The bottom plots of the figure illustrate the variations in the trajectory after 0.5 dimensionless time units. The bottom-left plot shows the variation of c_1 as a function of θ (the angle parameterizing the $\Delta\boldsymbol{v}$ direction). In the cases $\Delta_{0,1}$, this angle is computed as $\arctan(\Delta v_y/\Delta v_x)$. The same colorcode is used in all the plots in order to identify the same cases; the black asterisk corresponds to Δ_0, and the black circle to $\Delta\boldsymbol{v}_1$. Note that, as expected, Δ_1 is at the maximum/minimum points while Δ_0 is close to zero. Finally, the bottom-right plot illustrates the variation after 0.5 time units of each of the initial conditions. Here the circles correspond to the position $\phi_0 + \Delta$ projected on the saddle plane, and the asterisk corresponds to the position after 0.5 time units, also on the saddle plane; the arrows illustrate the variations each of these initial conditions experience. One can clearly observe the typical saddle behavior. The two black points and arrows correspond to Δ_0 and Δ_1. We must mention that these simulations have been done along different points in the orbit, and the same results are obtained.

Finally, we can perform the same analysis as in Sec. VI.A using these two thrust directions and compare the results to the set of Δ maneuvers in the xy plane. Figure 10 shows the relation between the magnitude of Δ and the jump on the saddle plane for the set of

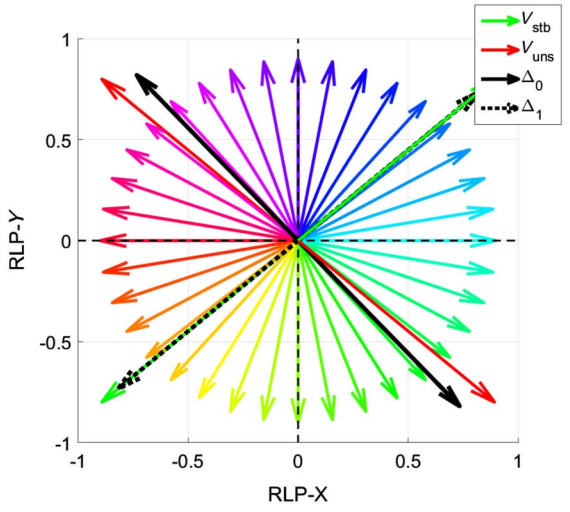

a) Projection of the velocity components of Δ on the xy plane

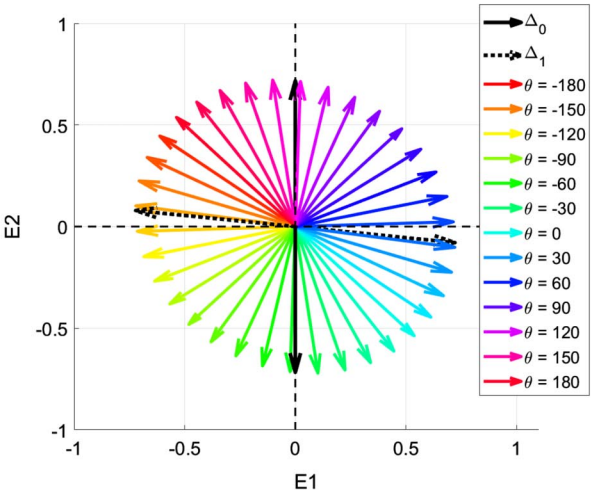

b) Projection of the velocity components of Δ on the saddle plane

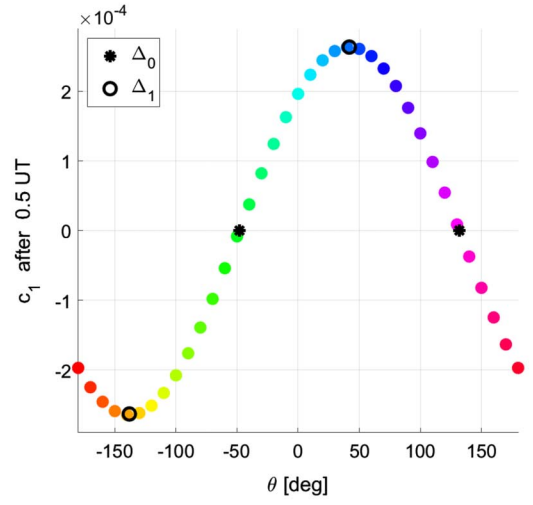

c) Variation of $c1$ as a function of the the angle θ= $\arctan(\Delta v_x/\Delta v_y)$

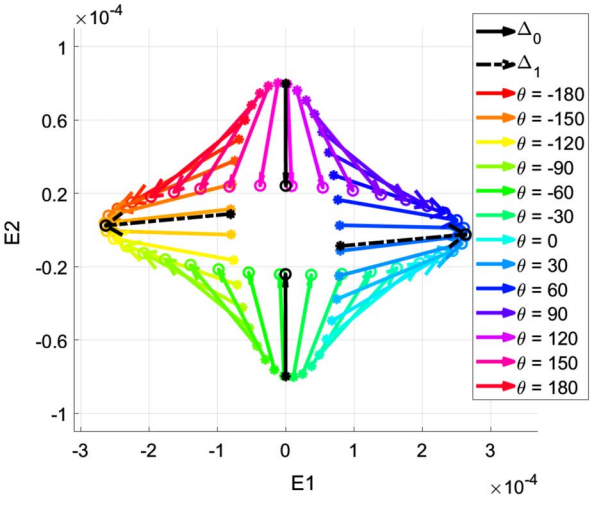

d) Variation of initial conditions (represented by ∘) after 0.5 time units (represented by ∗) on the saddle plane

Fig. 9 Different projections of Δ and variation of circle of initial conditions. Colorcode is used to identify the same cases through different plots.

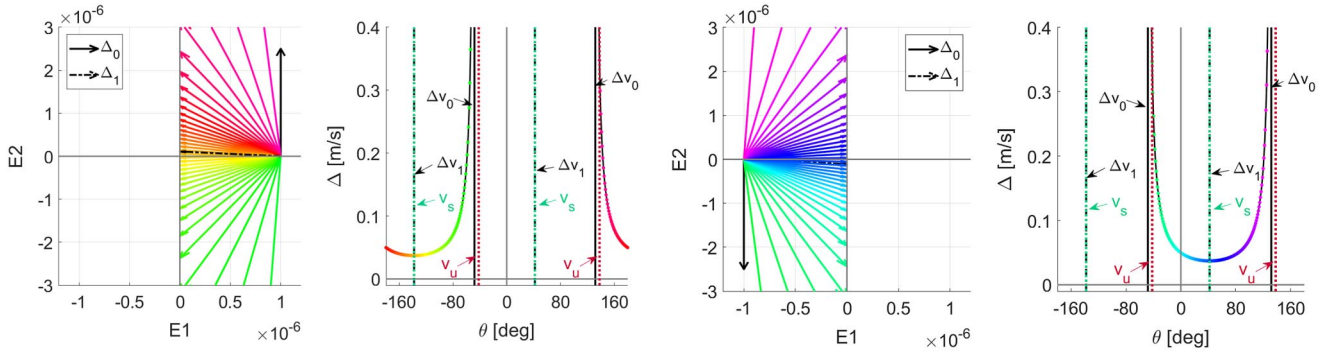

a) Initial condition on saddle plane at $(c_1, c_2) = (+10^{-6}, 0)$ b) Initial condition on saddle plane at $(c_1, c_2) = (-10^{-6}, 0)$

Fig. 10 Relation between the maneuver magnitude and the jump on the saddle plane. Left: Projection of Δ on the saddle plane. Right: Δ magnitude as a function of the $\theta = \arctan(\Delta v_y/\Delta v_x)$.

maneuvers in the xy plane and the Δ_0 and Δ_1 maneuvers. For each subplot, the two left plots show the projection on the saddle plane of the Δ found by the velocity constraint strategy, whereas the two plots on the right show the relation between the angle θ, which parameterizes the set of directions, and the Δ magnitude. We can see that the minimum maneuver size is at Δ_1, and that the magnitude tends to infinity when we reach Δ_0.

C. Effects of Changes in the Distance to the Nominal Orbit

In the previous sections, we have analyzed the variation of the maneuver magnitudes, as a function of the direction $\boldsymbol{u}$, for an initial displacement of 10^{-6} DU along the unstable direction. Here we show the results obtained considering an initial displacement from the periodic orbit along its unstable direction of $c_1 = 2 \times 10^{-6}, 3 \times 10^{-6}, 4 \times 10^{-6}$, and 5×10^{-6} DU, which correspond, approximately, to a distance of 300, 450, 600, and 750 km, respectively. To move away from the orbit, from the dynamic point of view, is equivalent to a delay in the execution of the maneuver or a large error in the insertion to a nominal orbit. The results are summarized in Figs. 11 and 12.

The plots in Fig. 11 show the variation of the different curves as a function of the angle θ that parameterizes the set $\boldsymbol{u} = (0, 0, 0, \cos\theta, \sin\theta, 0)^T$ of maneuver directions in the xy plane. The difference between the left plot and the right plot is the location of the initial condition on the saddle plane, being $(c_1, 0)$ for the left plot and $(-c_1, 0)$ for the right plot. Both plots show how the size of the maneuvers increases with the displacement along the unstable direction.

On the other hand, Fig. 12 shows the increase in the maneuvers size as a function on the distance to the nominal orbit (left) or as a function of the θ angle defining the thrust direction (middle and right). The left subplot shows the maneuver size for the minimum thrust direction ($\Delta_{\min}$) for each of the initial displacements along the unstable direction in kilometers. The maneuver size increases linearly as a function of the distance to the nominal orbit, with a slope of 2.48×10^{-4},

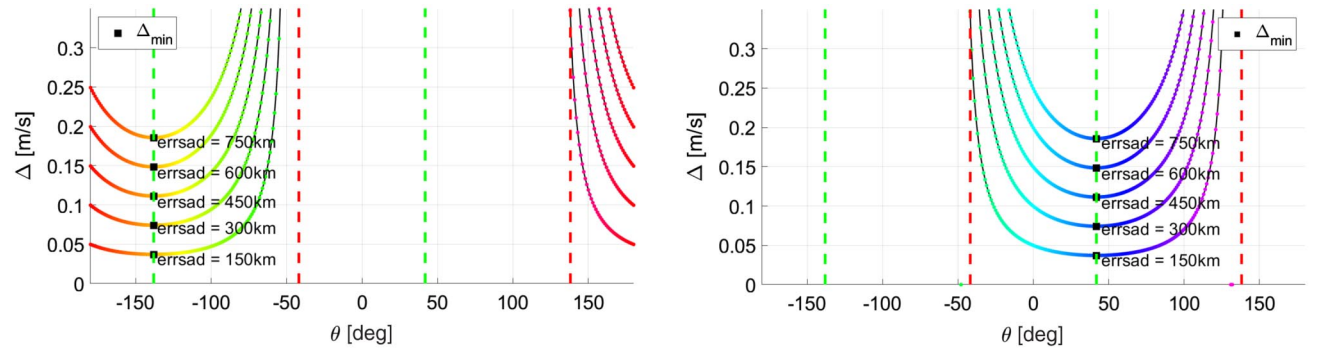

a) Δ increase as a function of θ for initial conditions on saddle plane at $(c_1, 0)$. b) Δ increase as a function of θ for initial conditions on saddle plane at $(-c_1, 0)$.

Fig. 11 Variation of Δ magnitude as a function of $\theta = \arctan(\Delta v_y/\Delta v_x)$. Each curve corresponds to a different initial displacement along the unstable direction.

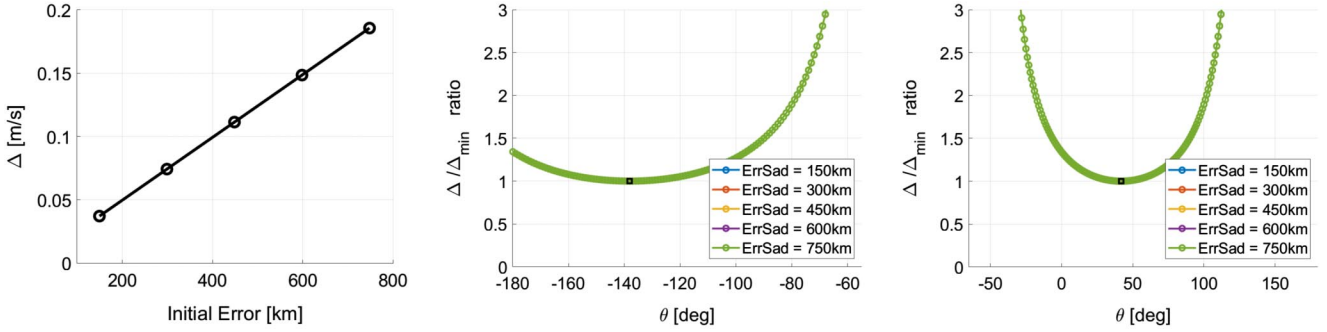

Fig. 12 Left: Minimum Δ magnitude as a function of the initial displacement (error) along the unstable direction. Middle and right: $\Delta/\Delta_{\min}$ ratio as a function of $\theta = \arctan(\Delta v_y/\Delta v_x)$.

presenting an increase of 2.48 cm/s for every increase of 100 km in the distance to the nominal orbit. The other two plots in Fig. 12 show, for all five different cases, the ratio between the Δ and $\Delta_{\min}$ maneuver magnitudes as a function of θ. Notice that this increase is the same for each of the initial displacements. We observe an exponential growth in the variation of the maneuver size as a function of θ. For instance, the deviation of 20° from the minimum $\Delta_{\min}$ has an increase of 1.05, whereas for 40° or 60° difference, the increase is 1.25 and 2.00, respectively. Thus, for this orbit, maneuver execution errors of up to 20° in the thrust direction do not have much impact on the controllability of the spacecraft.

These results show that there is a strict relation between the Δ maneuver size and the jump along a specific direction, in the saddle plane, to reach the stable mode. As seen in Sec. VI.D, this can be used to identify the minimum Δ magnitude in case of restrictions in the thrust direction.

D. Constraints on the Thrust Direction

Many missions have some type of thrust direction constraints for the station-keeping due to the spacecraft design and instruments requirements. Two examples of LPO missions with thrust constraints are JWST [15] and EUCLID [39]. For instance, JWST sun-shield must always be between the sun and the space telescope to keep the latter cold, making it unable to thrust toward the sun along the sun–telescope line. Similar to JWST, EUCLID must avoid illumination of the payload module to keep a thermal balance and ensure sufficient power from the solar panels, constraining again the thrust directions. As we will see here, projecting the thrust directions on the saddle plane generated by the Floquet modes allows us to understand the impact of these constraints on the Δ cost.

As an example, assume that the thrust vector of our spacecraft cannot point toward the sun, that is, $u_x > 0$. We can parameterize the thrust vector $\boldsymbol{u}$ with the pitch angle θ and the clock angle ψ having $\boldsymbol{u} = (0, 0, 0, \cos\theta, \sin\theta\cos\psi, \sin\theta\sin\psi)$. The thrust constraint $u_x > 0$ translates to $\theta \in [0, 90]°$ and $\psi \in [-180, 180]°$. Figure 13 shows the projection of $\boldsymbol{u}$ in the RLP reference frame (top) and on the saddle plane (bottom). The colorcode in the plots is used to identify vectors with the same pitch angle (left) and the same clock angle (right). Notice that most of the thrust directions in the saddle plane have $c_1 > 0$, having a limited set of thrust directions that ensure jumps in the saddle plane in the direction toward the sun.

We know that, given the relative position between the sun, the halo orbit at L_2, and the stable and unstable modes, trajectories that start at $\bar{\boldsymbol{e}}_1 > 0$ in the saddle plane drift toward the sun, whereas trajectories that start at $\bar{\boldsymbol{e}}_1 > 0$ drift away from the sun. Hence, in order to control a spacecraft that is drifting toward the sun, the projection of Δ in the FM must have $c_1 > 0$ (maneuver away from the sun [AS]), and, on the contrary, $c_1 < 0$ (maneuver toward the sun [TS]) if the spacecraft is escaping away from the sun. This is illustrated in Fig. 14, where the available thrust directions for each of these cases are highlighted. Notice that in case a TS maneuver is required, the jump in the saddle plane is limited to 45°, or above, from the $\bar{\boldsymbol{e}}_1$ axis, whereas the AS maneuvers have a wider range of possible directions, having thrust directions that align with $\bar{\boldsymbol{e}}_1$ and the minimum thrust direction (Sec. VI.B). From the results presented in Sec. VI.C, and given that TS maneuvers are limited to roughly 40° away from the minimum thrust direction ($\Delta_{\min}$), a ratio of 1.25 increase from the minimum thrust magnitude is expected for each TS maneuver.

Hence, a mission that wants to minimize the overall Δ cost of the mission should try to minimize the amount of TS maneuvers. This can be ensured by actively biasing down the AS maneuvers and biasing up in case of TS maneuvers, to ensure that the trajectory remains always at $\bar{\boldsymbol{e}}_1 < 0$ in the saddle projection. A schematics of this strategy is depicted in Fig. 15, where we see the impact of biasing a Δ maneuver in the saddle plan. The size of the active bias will vary for each mission, and should account for different sources of perturbations, such as solar radiation pressure, maneuver execution errors, momentum unloads, and orbit determination errors.

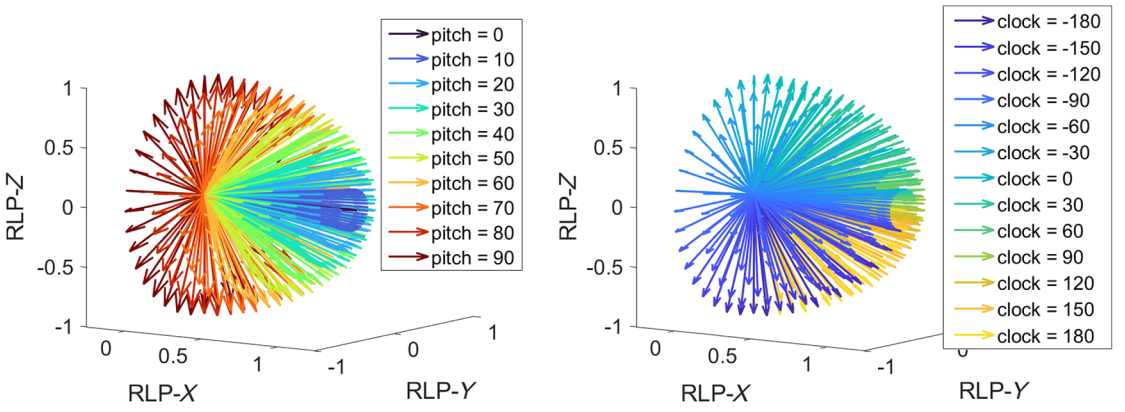

a) Projection of the velocity components of u on the RLP frame

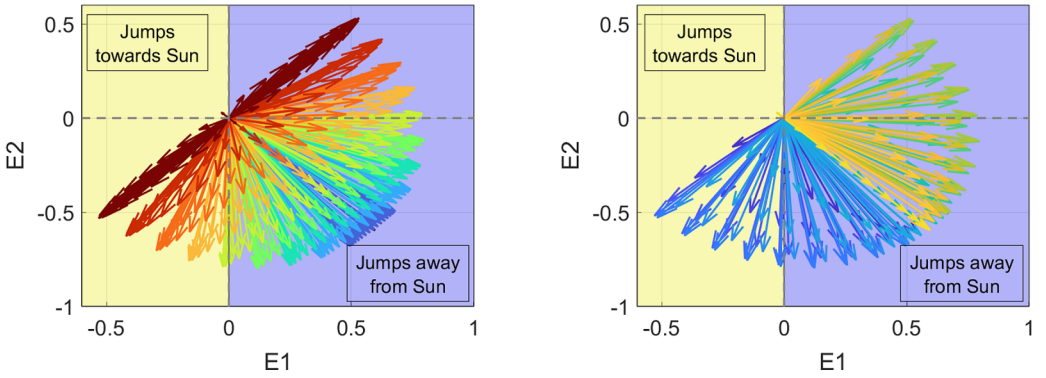

b) Projection of the velocity components of u on the saddle plane $\bar{e}_1, \bar{e}_2$

Fig. 13 Different projections of the thrust vectors $\boldsymbol{u} = (0,0,0, \cos\theta, \sin\theta\cos\psi, \sin\theta\sin\psi)$. The colorcode groups same pitch angle θ (left) and same clock angle ψ (right) directions.

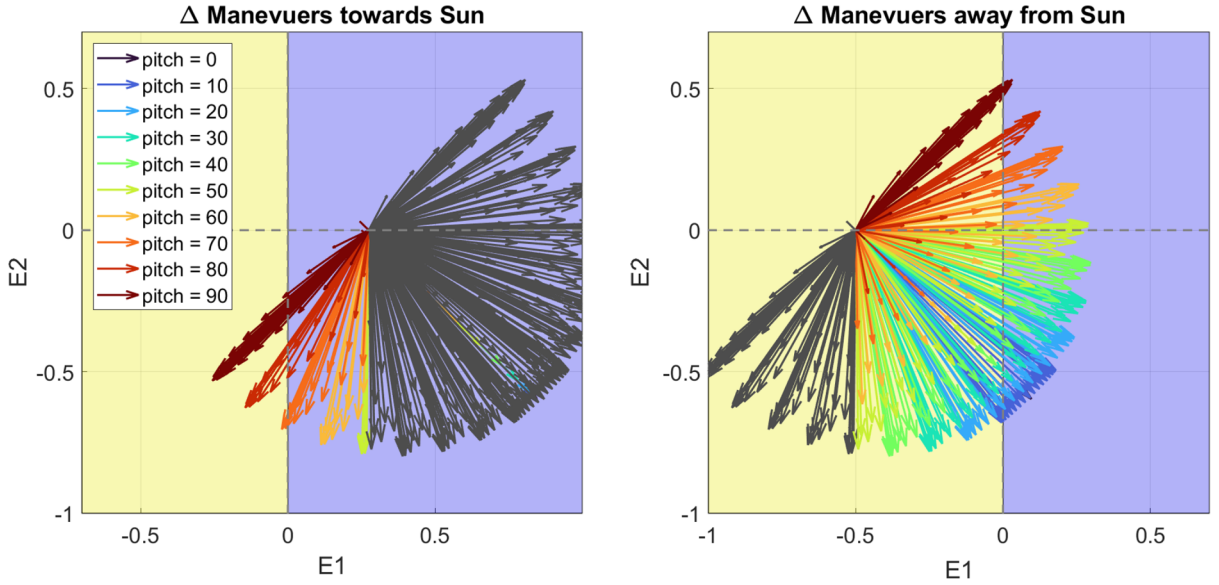

a) Highlight of the set of available thrust directions for maneuvers towards the Sun

b) Highlight of the set of available thrust directions away from the Sun

Fig. 14 Projection of the thrust direction as a function of the pitch angle on the saddle plane.

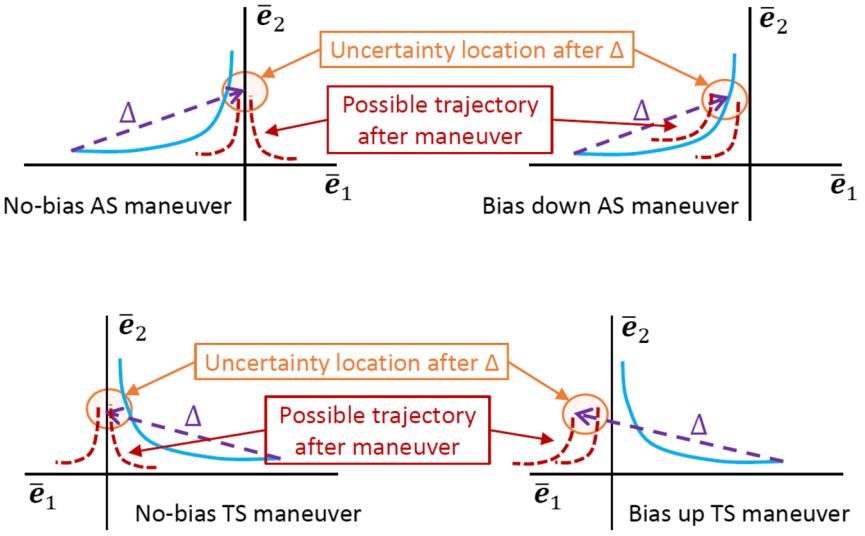

Fig. 15 Schematic representation of the biasing strategy to ensure having AS maneuvers.

VII. Conclusions

In this paper, two different station-keeping strategies have been compared from a geometrical point of view: the Floquet mode approach, and the velocity constraint at the plane crossing approach. Despite following different procedures, both strategies cancel the unstable mode and provide the same maneuver magnitudes if they are forced to thrust along the same direction.

A basic tool for the analysis has been the use of the jet transport technique, which has enabled us to compare both strategies from a semi-analytic point of view, computing the second-order Taylor expansion of the Poincaré maps associated to both strategies. Comparing the Taylor coefficients of the Poincaré map, both strategies are the same up to second order. This technique has also been used to study the stability and long-term behavior of the controllers showing that both controllers stabilize the motion of the spacecraft around the reference periodic orbit.

A geometric explanation has also been given to the behavior of these station-keeping strategies. The projection of the thrust direction on the saddle plane (plane generated by the unstable and stable Floquet modes) determines the maneuver magnitude, as the magnitude required to control the satellite is related to a jump on the saddle plane along the thrust direction to cancel the unstable mode.

Using this information, the directions that provide the minimum and maximum maneuver magnitudes can be determined. The directions whose projections on the saddle plane give small variation in the unstable mode will result in large maneuvers. On the other hand, the directions whose projections on the saddle plane produce large variations of the unstable mode will result in small maneuvers, allowing the determination of the suitable maneuver directions. This enables us to have a way to search for the optimal maneuvers in the case of having constraints on the thrust vector direction.

Moreover, the geometric interpretation of station-keeping strategies has been used to show how constraints in the thrust direction impact the maneuver magnitudes on the example of a spacecraft that can only thrust away from the sun. Moreover, this interpretation can be used to envision strategies that help mitigate the impact of these constraints, such as actively biasing the maneuvers to ensure that we remain on the suitable side of the saddle plane.

Finally, this geometric way of interpreting the station-keeping strategies can also be used to better understanding how orbit determination or maneuver execution errors affect the controllability of the spacecraft around an LPO. For instance, planned station-keeping

maneuver cancels the unstable mode placing the spacecraft close to the stable manifold. Due to maneuver execution errors the applied maneuver will fail to completely cancel the unstable mode. However, if these errors are small, the spacecraft will be close to the stable manifold, and its trajectory will remain close to the reference orbit. Knowledge on maneuver executions error will allow estimates on how far we are from the stable mode and evaluate the effectiveness of the maneuver.

Appendix: Tables with the Coefficients of the $\mathcal{P}_{F0}$ Maps Taylor Expansion

Taylor expansion of $\mathcal{P}_{F0}$ up to second order

$\mathcal{P}_{F0}$	x_f	z_f	$\dot{x}_f$	$\dot{y}_f$	$\dot{z}_f$
δx_0	1.6011e − 01	−2.5865e − 02	6.2671e − 03	−8.5184e − 01	−1.5318e − 01
δz_0	−6.4870e − 02	9.9488e − 01	−3.1216e − 03	−6.3744e − 02	5.8085e − 02
$\delta \dot{x}_0$	1.3832e − 01	4.7256e − 03	−3.1484e − 03	−7.4908e − 01	6.6291e − 02
$\delta \dot{y}_0$	−1.5539e − 01	−1.4854e − 04	6.5125e − 03	8.3936e − 01	−1.3214e − 01
$\delta \dot{z}_0$	3.8161e − 03	−8.8954e − 02	−5.1458e − 02	1.6444e − 02	9.9743e − 01
δx_0^2	−1.9600e + 01	1.8347e + 00	1.9300e + 00	9.9589e + 01	−4.0833e + 01
$\delta x_0 \delta z_0$	4.2809e + 00	−3.8696e + 01	1.0668e + 01	1.6739e + 01	−3.5182e + 01
$\delta x_0 \delta \dot{x}_0$	7.8816e + 00	1.4280e + 00	9.5593e − 01	−5.0224e + 01	−1.8505e + 01
$\delta x_0 \delta \dot{y}_0$	−8.7173e + 00	−3.6885e + 00	−1.0709e + 00	5.6272e + 01	1.8158e + 01
$\delta x_0 \delta \dot{z}_0$	−2.1446e + 00	3.6022e + 01	−2.5559e − 02	1.1784e + 00	4.4913e + 01
δz_0^2	−3.5738e + 01	−9.7141e + 00	−8.8287e + 00	−3.0433e + 01	1.0587e + 02
$\delta z_0 \delta \dot{x}_0$	8.5342e − 01	2.2400e + 00	−8.8481e + 00	2.2045e + 00	1.0016e + 02
$\delta z_0 \delta \dot{y}_0$	−1.2296e + 00	−1.9548e + 00	1.3175e + 01	−3.4401e + 00	−1.1211e + 02
$\delta z_0 \delta \dot{z}_0$	4.6991e + 00	−9.6328e + 00	−5.6087e + 01	1.6696e + 01	−4.2857e + 00
$\delta \dot{x}_0^2$	−1.4718e + 00	−1.4625e − 02	1.8504e − 01	4.6379e + 00	−2.2288e + 00
$\delta \dot{x}_0 \delta \dot{y}_0$	3.2378e + 00	5.0227e − 01	−5.3416e − 01	−1.0053e + 01	5.6643e + 00
$\delta \dot{x}_0 \delta \dot{z}_0$	1.1109e + 00	−8.1047e + 00	2.0545e + 00	−6.0855e + 00	−1.1462e + 01
$\delta \dot{y}_0^2$	−1.7906e + 00	−5.4470e − 01	3.8324e − 01	5.4205e + 00	−3.5494e + 00
$\delta \dot{y}_0 \delta \dot{z}_0$	−8.7865e − 01	9.0798e + 00	−2.8875e + 00	7.5356e + 00	1.2856e + 01
$\delta \dot{z}_0^2$	−3.1724e + 00	1.0290e − 01	5.0310e + 00	−6.1195e + 00	1.4830e − 02

Taylor expansion of $\mathcal{P}_{Ff}$ up to second order

$\mathcal{P}_{Ff}$	x_f	z_f	$\dot{x}_f$	$\dot{y}_f$	$\dot{z}_f$
δx_0	1.6011e − 01	−2.5865e − 02	6.2692e − 03	−8.5184e − 01	−1.5318e − 01
δz_0	−6.4871e − 02	9.9488e − 01	−3.1257e − 03	−6.3743e − 02	5.8085e − 02
$\delta \dot{x}_0$	1.3832e − 01	4.7256e − 03	−3.1529e − 03	−7.4908e − 01	6.6291e − 02
$\delta \dot{y}_0$	−1.5538e − 01	−1.4850e − 04	6.5193e − 03	8.3936e − 01	−1.3214e − 01
$\delta \dot{z}_0$	3.8088e − 03	−8.8955e − 02	−5.1489e − 02	1.6449e − 02	9.9743e − 01
δx_0^2	−1.9599e + 01	1.8348e + 00	1.9330e + 00	9.9589e + 01	−4.0833e + 01
$\delta x_0 \delta z_0$	4.2793e + 00	−3.8697e + 01	1.0663e + 01	1.6741e + 01	−3.5181e + 01
$\delta x_0 \delta \dot{x}_0$	7.8832e + 00	1.4280e + 00	9.5895e − 01	−5.0224e + 01	−1.8505e + 01
$\delta x_0 \delta \dot{y}_0$	−8.7181e + 00	−3.6885e + 00	−1.0743e + 00	5.6273e + 01	1.8158e + 01
$\delta x_0 \delta \dot{z}_0$	−2.1445e + 00	3.6022e + 01	−2.5171e − 02	1.1773e + 00	4.4913e + 01
δz_0^2	−3.5727e + 01	−9.7141e + 00	−8.7775e + 00	−3.0434e + 01	1.0588e + 02
$\delta z_0 \delta \dot{x}_0$	8.5040e − 01	2.2399e + 00	−8.8593e + 00	2.2080e + 00	1.0016e + 02
$\delta z_0 \delta \dot{y}_0$	−1.2257e + 00	−1.9547e + 00	1.3189e + 01	−3.4443e + 00	−1.1211e + 02
$\delta z_0 \delta \dot{z}_0$	4.6905e + 00	−9.6331e + 00	−5.6123e + 01	1.6701e + 01	−4.2898e + 00
$\delta \dot{x}_0^2$	−1.4715e + 00	−1.4619e − 02	1.8655e − 01	4.6376e + 00	−2.2287e + 00
$\delta \dot{x}_0 \delta \dot{y}_0$	3.2369e + 00	5.0226e − 01	−5.3783e − 01	−1.0052e + 01	5.6642e + 00
$\delta \dot{x}_0 \delta \dot{z}_0$	1.1122e + 00	−8.1046e + 00	2.0594e + 00	−6.0880e + 00	−1.1462e + 01
$\delta \dot{y}_0^2$	−1.7901e + 00	−5.4468e − 01	3.8549e − 01	5.4199e + 00	−3.5494e + 00
$\delta \dot{y}_0 \delta \dot{z}_0$	−8.8049e − 01	9.0798e + 00	−2.8943e + 00	7.5388e + 00	1.2856e + 01
$\delta \dot{z}_0^2$	−3.1694e + 00	1.0298e − 01	5.0424e + 00	−6.1227e + 00	1.5345e − 02

Taylor expansion of $\mathcal{P}_{F0}$ up to second order

$\mathcal{P}_{F0}$	x_f	z_f	$\dot{x}_f$	$\dot{y}_f$	$\dot{z}_f$
δx_0	1.6011e − 01	−2.5865e − 02	6.2692e − 03	−8.5184e − 01	−1.5318e − 01
δz_0	−6.4871e − 02	9.9488e − 01	−3.1257e − 03	−6.3743e − 02	5.8085e − 02
$\delta \dot{x}_0$	1.3832e − 01	4.7256e − 03	−3.1529e − 03	−7.4908e − 01	6.6291e − 02
$\delta \dot{y}_0$	−1.5538e − 01	−1.4850e − 04	6.5193e − 03	8.3936e − 01	−1.3214e − 01
$\delta \dot{z}_0$	3.8088e − 03	−8.8955e − 02	−5.1489e − 02	1.6449e − 02	9.9743e − 01
δx_0^2	−6.2909e + 01	2.4032e + 01	3.6221e + 01	3.5710e + 02	−1.8233e + 02
$\delta x_0 \delta z_0$	−2.0631e + 01	−2.5502e + 01	−7.1240e + 00	1.0800e + 02	−8.3608e + 01

Appendix (*Continued.*)

Taylor expansion of $\mathcal{P}_{F0}$ up to second order					
$\mathcal{P}_{F0}$	x_f	z_f	$\dot{x}_f$	$\dot{y}_f$	$\dot{z}_f$
$\delta x_0\delta\dot{x}_0$	1.6386e + 01	6.4525e − 01	5.2769e + 01	−3.2554e + 01	−1.6246e + 01
$\delta x_0\delta\dot{y}_0$	−1.9386e + 01	−3.0020e + 00	−6.1121e + 01	4.0943e + 01	1.6048e + 01
$\delta x_0\delta\dot{z}_0$	1.7337e + 01	3.9329e + 01	3.3233e + 01	−7.6373e + 01	3.7580e + 01
δz_0^2	3.7466e + 01	−5.2449e + 01	2.3291e + 02	−1.7925e + 01	1.2538e + 02
$\delta z_0\delta\dot{x}_0$	−3.7084e + 00	2.0392e + 00	−9.9214e + 00	2.8032e + 01	9.7680e + 01
$\delta z_0\delta\dot{y}_0$	3.8962e + 00	−1.1126e + 00	1.5815e + 01	−3.2288e + 01	−1.1051e + 02
$\delta z_0\delta\dot{z}_0$	4.5551e + 00	−2.0283e + 01	−8.0886e + 01	1.4537e + 01	1.6150e + 01
$\delta\dot{x}_0^2$	2.3506e + 00	−1.5505e + 00	3.4630e + 01	2.7267e + 01	8.8553e + 00
$\delta\dot{x}_0\delta\dot{y}_0$	−4.8494e + 00	4.0614e + 00	−8.5003e + 01	−7.2278e + 01	−2.1167e + 01
$\delta\dot{x}_0\delta\dot{z}_0$	−7.3243e + 00	−1.0062e + 01	1.2615e + 02	1.9167e + 02	2.2426e + 01
$\delta\dot{y}_0^2$	2.5338e + 00	−2.6195e + 00	5.2668e + 01	4.7469e + 01	1.2791e + 01
$\delta\dot{y}_0\delta\dot{z}_0$	6.4305e + 00	1.1791e + 01	−1.7229e + 02	−2.3920e + 02	−3.1734e + 01
$\delta\dot{z}_0^2$	1.5416e + 01	−4.3474e + 00	2.6574e + 02	2.0882e + 02	5.6775e + 01

Acknowledgments

The work has been funded under the Goddard Planetary Heliophysics Institute Task 595.001 in collaboration with the University of Maryland Baltimore County under the NNG11PL02A. Chen Gao thanks the support of Chinese Scholarship Council. Josep J. Masdemont thanks MINECO-FEDER for the grant PGC2018-100928-B-100 and the Catalan government for the grant 2017SGR-1049. Gerard Gómez thanks the Catalan grant government 2017SGR-1374, and MINECO-FEDER for the grant PID2019-104851GB-I00. The authors are grateful for the valuable suggestions of the reviewers.

References

[1] Farquhar, R., "The Control and Use of Libration Point Satellites," Ph.D. Thesis, Stanford Univ., 1969.

[2] Breakwell, J., Kamel, A., and Ratner, M., "Station-Keeping for a Translunar Communications Station," *Celestial Mechanics*, Vol. 10, No. 3, Sept. 1974, pp. 357–373. https://doi.org/10.1007/BF01586864

[3] Farquhar, R., Muhonen, D., Newman, C., and Heuberger, H., "The First Libration Point Satellite. Mission Overview and Flight History," *AAS/AIAA Astrodynamics Specialist Conference*, AAS Paper 79–126, 1979.

[4] Muhonen, D., "Accelerometer Enhanced Orbit Control Near the Sun-Earth L_1 Libration Point," *Space Flight Mechanics, Science and Technology Series*, AIAA Paper 1983-0018, 1983. https://doi.org/10.2514/6.1983-18

[5] Rodrguez-Canabal, J., "Operational Halo Orbit Maintenance Technique for SOHO," ESA Special Publication, Darmstadt, Germany, Vol. 255, 1986, pp. 71–78.

[6] Simó, C., Gómez, G., Llibre, J., and Martnez, R., "Station Keeping of a Quasiperiodic Halo Orbit Using Invariant Manifolds," ESA Special Publication, Darmstadt, Germany, Vol. 255, 1986, pp. 65–70.

[7] Simó, C., Gómez, G., Llibre, J., Martnez, R., and Rodrquez, R., "On the Optimal Station Keeping Control of Halo Orbits," *Acta Astronautica*, Vol. 15, Nos. 6–7, June–July 1987, pp. 391–397. https://doi.org/10.1016/0094-5765(87)90175-5

[8] Howell, K., and Gordon, S., "Orbit Determination Error Analysis and a Station-Keeping Strategy for Sun–Earth L_1 libration point orbits," *Journal of the Astronautical Sciences*, Vol. 42, No. 2, April 1994, pp. 207–228.

[9] Howell, K., and Pernicka, H., "Stationkeeping Method for Libration Point Trajectories," *Journal of Guidance, Control, and Dynamics*, Vol. 16, No. 1, Jan.–Feb. 1993, pp. 151–159. https://doi.org/10.2514/3.11440.

[10] Keeter, T., "Station-Keeping Strategies for Libration Point Orbits: Target Point and Floquet Mode Approaches," Master's Thesis, School of Aeronautics and Astronautics, Purdue Univ., West Lafayette, IN, 1994.

[11] Roberts, C., "Long-Term Missions at the Sun-Earth Libration Point L1: ACE, SOHO, and WIND," *ASS Astrodynamics Specialist Conference*, AAS Paper 11-485, 2011.

[12] Brown, J., and Petersen, J., "Applying Dynamical Systems Theory to Optimize Libration Point Orbit Stationkeeping Maneuvers for Wind," *AIAA/AAS Astrodynamics Specialist Conference*, AIAA Paper 2014-4304, 2014. https://doi.org/10.2514/6.2014-4304

[13] Folta, D., Pavlak, T., Haapala, A., Howell, K., and Woodard, M., "Earth-Moon Libration Point Orbit Stationkeeping: Theory, Modeling, and Operations," *Acta Astronautica*, Vol. 94, No. 4, Aug. 2014, pp. 421–433. https://doi.org/10.1016/j.actaastro.2013.01.022

[14] Folta, D., Pavlak, T., Howell, K., Woodard, M., and Woodfork, W., "Stationkeeping of Lissajous Trajectories in the Earth-Moon System with Applications to ARTEMIS," *AAS/AIAA Spaceflight Mechanics Meeting*, AAS Paper 10-113, 2010.

[15] Petersen, J., "L2 Station Keeping Maneuver Strategy for the James Webb Space Telescope," *AAS/AIAA Astrodynamics Specialist Conference*, AAS Paper 19-806, 2019.

[16] Bosanac, N., Webster, C., Howell, K., and Folta, D., "Trajectory Design for the Wide Field Infrared Survey Telescope Mission," *Journal of Guidance, Control, and Dynamics*, Vol. 42, No. 9, April 2019, pp. 1899–1911. https://doi.org/10.2514/1.G004179

[17] Farrés, A., Webster, C., Donaldson, J., and Folta, D., "Orbital Maintenance for the Wide Field Infrared Survey Telescope: The Effects of Solar Radiation Pressure and Navigation Accuracies on Station Keeping," *AAS/AIAA Astrodynamics Specialist Conference*, AAS Paper 18-434, 2018.

[18] Folta, D., and Vaugh, F., "A Survey of Earth-Moon Libration Orbits: Stationkeeping Strategies and Intra-Orbit Transfers," *AIAA/Astrodynamics Specialist Conference*, AIAA Paper 2004-4741, 2004. https://doi.org/10.2514/6.2004-4741

[19] Gómez, G., Howel, K., Masdemont, J., and Simó, C., "Station-Keeping Strategies for Translunar Libration Point Orbits," *AAS/AIAA Space Flight Mechanics Meeting*, AAS Paper 98-168, 1998.

[20] Shirobokov, M., Trofimov, S., and Ovchinnikov, M., "Survey of Station-Keeping Techniques for Libration Point Orbits," *Journal of Guidance, Control, and Dynamics*, Vol. 40, No. 5, Jan. 2017, pp. 1850–1871. https://doi.org/10.2514/1.G001850

[21] Pérez-Palau, D., Masdemont, J., and Gómez, G., "Tools to Detect Structures in Dynamical Systems Using Jet Transport," *Celestial Mechanics and Dynamical Astronomy*, Vol. 123, No. 3, Aug. 2015, pp. 239–262. https://doi.org/10.1007/s10569-015-9634-3

[22] Pérez-Palau, D., "Dynamical Transport Mechanisms in Celestial Mechanics and Astrodynamics Problems," Ph.D. Thesis, Univ. de Barcelona, Barcelona, 2016.

[23] Szebehely, V., *Theory of Orbits*, Academic Press, New York, 1967, pp. 7–40, Chap. 1. https://doi.org/10.1016/B978-0-12-395732-0.X5001-6

[24] Richardson, D., "A Note on the Lagrangian Formulation for Motion About the Collinear Points," *Celestial Mechanics*, Vol. 22, No. 3, Jan. 1980, pp. 231–235. https://doi.org/10.1007/BF01229509

[25] Richardson, D., "Analytical Construction of Periodic Orbits About the Collinear Points," *Celestial Mechanics*, Vol. 22, No. 3, Oct. 1980, pp. 241–253.
https://doi.org/10.1007/BF01229511

[26] Farquhar, R., and Kamel, A., "Quasi-Periodic Orbits About the Translunar Libration Point," *Celestial Mechanics*, Vol. 7, No. 4, June 1973, pp. 458–473.
https://doi.org/10.1007/BF01227511

[27] Richardson, D., and Cary, N., "A Uniformly Valid Solution for Motion About the Interior Libration Point of the Perturbed Elliptic-Restricted Problem," *AAS/AIAA Astrodynamics Specialist Conference*, AAS Paper 75-021, 1975.

[28] Gómez, G., Jorba, A., Masdemont, J., and Simó, C., "Study Refinement of Semi-Analytical Halo Orbit Theory," European Space Operation Center (ESOC), ESOC Contract 8625/89/D/MD(SC), Darmstadt, Germany, 1991.

[29] Gómez, G., Masdemont, J., and Simó, C., "Quasihalo Orbits Associated with Libration Points," *Journal of the Astronautical Sciences*, Vol. 46, No. 2, June 1998, pp. 1–42.
https://doi.org/10.1007/BF03546241

[30] Roberts, C., Case, S., Reagoso, J., and Webster, C., "Early Mission Maneuver Operations for the Deep Space Climate Observatory Sun-Earth L1 Libration Point Mission," *AAS/AIAA Astrodynamics Specialist Conference*, AAS Paper 15-613, 2015.

[31] Gómez, G., Lo, M., Masdemont, J., and Museth, K., "Simulation of Formation Flight Near L_2 for the TPF Mission," *ASS/AIAA Astrodynamics Specialist Conference*, AAS Paper 01-305, 2001.

[32] Jorba, A., Ramírez-Ros, R., and Villanueva, J., "Effective Reducibility of Quasi-periodic Linear Equations Close to Constant Coefficients," *SIAM Journal on Mathematical Analysis*, Vol. 28, No. 1, Jan. 1997, pp. 178–188.
https://doi.org/10.1137/S0036141095280967

[33] Farres, A., and Jorba, À., "A Dynamical System Approach for the Station Keeping of a Solar Sail," *Journal of the Astronautical Science*, Vol. 56, No. 2, June 2008, pp. 199–230.
https://doi.org/10.1007/BF03256549

[34] Farres, A., and Jorba, À., "Station Keeping of a Solar Sail Around a Halo Orbit," *Acta Astronautica*, Vol. 94, No. 1, Feb. 2014, pp. 527–539.
https://doi.org/10.1016/j.actaastro.2012.07.002

[35] Gómez, G., Llibre, J., Martnez, R., and Simó, C., *Dynamics and Mission Design Near Libration Point Orbits—Volume 1: Fundamentals: The Case of Collinear Libration Points*, World Scientific, Singapore, 2001, pp. 143–184.
https://doi.org/10.1142/4402

[36] Gómez, G., Jorba, À., Masdemont, J., and Simó, C., *Dynamics and Mission Design Near Libration Point Orbits—Volume 3: Advanced Methods for Collinear Points*, World Scientific, Singapore, 2001, pp. 33–66.
https://doi.org/10.1142/4337

[37] Grote, J., Makino, K., and Berz, M., "High-Order Validated Representation of Poincaré Maps," *Proceedings of the 5th WSEAS/IASME, International Conference on Systems Theory and Scientific Computation*, World Scientific, Singapore, 2005, pp. 324–329.

[38] Grote, J., Berz, M., and Makino, K., "High-Order Representation of Poincaré Maps," *Nuclear Instruments and Methods in Physics Research A*, Vol. 558, 2006, pp. 106–111.
https://doi.org/10.1007/3-540-28438-9_5

[39] Renk, F., and Landgraf, M., "EUCLID: ESA's Dark Energy 3-Axis Stabilized Survey Mission at the Night-Side Sun-Earth Libration Point," *24th International Symposium on Space Flight Dynamics*, APL (Johns Hopkins University Applied Physics Laboratory), 2014, Paper S6-6.